Metadata of the chapter that will be visualized in SpringerLink

Book Title	Plasticity, Damage and Fracture in Advanced Materials	
Series Title		
Chapter Title	Damage Identification Supported by Nondestructive Testing Techniques	
Copyright Year	2019	
Copyright HolderName	Springer Nature Switzerland AG	
Corresponding Author	Family Name	**Kowalewski**
	Particle	
	Given Name	**Zbigniew L.**
	Prefix	
	Suffix	
	Role	
	Division	
	Organization	Institute of Fundamental Technological Research
	Address	ul. Pawińskiego 5B, 02-106, Warsaw, Poland
	Email	zkowalew@ippt.pan.pl
Author	Family Name	**Ustrzycka**
	Particle	
	Given Name	**Aneta**
	Prefix	
	Suffix	
	Role	
	Division	
	Organization	Institute of Fundamental Technological Research
	Address	ul. Pawińskiego 5B, 02-106, Warsaw, Poland
	Email	austrzyc@ippt.pan.pl
Author	Family Name	**Szymczak**
	Particle	
	Given Name	**Tadeusz**
	Prefix	
	Suffix	
	Role	
	Division	
	Organization	Motor Transport Institute
	Address	ul. Jagiellonska 80, 03-301, Warsaw, Poland
	Email	tadeusz.szymczak@its.waw.pl
Author	Family Name	**Makowska**
	Particle	
	Given Name	**Katarzyna**
	Prefix	
	Suffix	

	Role	
	Division	
	Organization	Motor Transport Institute
	Address	ul. Jagiellonska 80, 03-301, Warsaw, Poland
	Email	katarzyna.makowska@its.waw.pl
Author	Family Name	**Kukla**
	Particle	
	Given Name	**Dominik**
	Prefix	
	Suffix	
	Role	
	Division	
	Organization	Institute of Fundamental Technological Research
	Address	ul. Pawińskiego 5B, 02-106, Warsaw, Poland
	Email	dkukla@ippt.pan.pl

Abstract

Development of damage due to exploitation loadings was investigated using destructive and non-destructive methods in materials commonly applied in power engineering or automotive industry. The fatigue or creep tests for a range of different materials were interrupted for selected number of cycles or deformation level in order to assess a damage degree. As destructive methods the standard tensile tests were carried out after prestraining. Subsequently, an evolution of the selected tensile parameters was taken into account for damage identification. The ultrasonic, magnetic and novel optical techniques were used as the non-destructive methods for damage evaluation. The experimental programme also included microscopic observations. The results show that ultrasonic and magnetic parameters can be correlated with those coming from destructive tests. It is shown that good correlation of mechanical and selected non-destructive parameters identifying damage can be achieved for the materials tested. The results of damage monitoring during fatigue tests supported by contemporary optical techniques (Digital Image Correlation and Electronic Spackle Pattern Interferometry) proved their great suitability for effective identification of places of damage initiation.

The work additionally presents simulation of fatigue crack initiation for cyclic loading within the nominal elastic regime. It is assumed that damage growth occurs due to action of mean stress and its fluctuations induced by crystalline grain inhomogeneity and free boundary effect. The fluctuation fields in polycrystalline metal subjected to the mechanical loading inducing uniform mean stress and strain states development due to the material inhomogeneity related to grain anisotropy and inhomogeneity. The yielding process develops at the low mean stress level in some grains due to the local strain accumulation at their boundaries. These stress fluctuations, developing at a fraction of the macroscopic elastic limit, are the source of initial structural defects and microscopic plastic mechanisms controlling the evolution of defect assemble toward the state of advanced yielding. A mechanism responsible for damage accumulation during cyclic loading below the yield point remains elusive and requires classification. The analytical description is aimed at development of the consistent description of the microplastic state of material. The macrocrack initiation corresponds to a critical value of accumulated damage.

Keywords

Creep - Damage - Fatigue - Optical methods (DIC - ESPI) - Nondestructive investigations - Magnetic and ultrasonic techniques - Microplasticity - Crack - Modelling

Chapter 6
Damage Identification Supported by Nondestructive Testing Techniques

Zbigniew L. Kowalewski, Aneta Ustrzycka, Tadeusz Szymczak, Katarzyna Makowska, and Dominik Kukla

Abstract Development of damage due to exploitation loadings was investigated using destructive and non-destructive methods in materials commonly applied in power engineering or automotive industry. The fatigue or creep tests for a range of different materials were interrupted for selected number of cycles or deformation level in order to assess a damage degree. As destructive methods the standard tensile tests were carried out after prestraining. Subsequently, an evolution of the selected tensile parameters was taken into account for damage identification. The ultrasonic, magnetic and novel optical techniques were used as the non-destructive methods for damage evaluation. The experimental programme also included microscopic observations. The results show that ultrasonic and magnetic parameters can be correlated with those coming from destructive tests. It is shown that good correlation of mechanical and selected non-destructive parameters identifying damage can be achieved for the materials tested. The results of damage monitoring during fatigue tests supported by contemporary optical techniques (Digital Image Correlation and Electronic Spackle Pattern Interferometry) proved their great suitability for effective identification of places of damage initiation.

The work additionally presents simulation of fatigue crack initiation for cyclic loading within the nominal elastic regime. It is assumed that damage growth occurs due to action of mean stress and its fluctuations induced by crystalline grain inhomogeneity and free boundary effect. The fluctuation fields in polycrystalline metal subjected to the mechanical loading inducing uniform mean stress and strain states development due to the material inhomogeneity related to grain anisotropy and inhomogeneity. The yielding process develops at the low mean stress level in some grains due to the local strain accumulation at their boundaries. These stress fluctuations,

Zbigniew L. Kowalewski · Aneta Ustrzycka · Dominik Kukla
Institute of Fundamental Technological Research, ul. Pawińskiego 5B, 02-106 Warsaw, Poland,
e-mail: zkowalew@ippt.pan.pl, austrzyc@ippt.pan.pl, dkukla@ippt.pan.pl

Tadeusz Szymczak · Katarzyna Makowska
Motor Transport Institute ul. Jagiellonska 80, 03-301 Warsaw, Poland,
e-mail: tadeusz.szymczak@its.waw.pl, katarzyna.makowska@its.waw.pl

H. Altenbach et al. (eds.), *Plasticity, Damage and Fracture in Advanced Materials*, Advanced Structured Materials 121,
https://doi.org/10.1007/978-3-030-34851-9_6

developing at a fraction of the macroscopic elastic limit, are the source of initial structural defects and microscopic plastic mechanisms controlling the evolution of defect assemble toward the state of advanced yielding. A mechanism responsible for damage accumulation during cyclic loading below the yield point remains elusive and requires classification. The analytical description is aimed at development of the consistent description of the microplastic state of material. The macrocrack initiation corresponds to a critical value of accumulated damage.

Key words: Creep · Damage · Fatigue · Optical methods (DIC, ESPI) · Nondestructive investigations · Magnetic and ultrasonic techniques · Microplasticity · Crack · Modelling

6.1 Introduction

In majority cases, degradation of a material has a local character and it is based on damage development leading to generation of cracks appearing around structural defects or geometrical notches. An identification of these areas and their subsequent monitoring requires a full-field displacement measurements performed on the objects surfaces. This chapter presents an attempt to use the Electronic Speckle Pattern Interferometry (ESPI) and Digital Image Correlation (DIC) for damage evaluation and its monitoring on specimens made of different materials subjected to static, monotonic or cyclic loading. Also effectiveness of other nondestructive techniques will be discussed. Among them one can indicate magnetic and ultrasonic methods.

Determination of material behaviour under various loading types can be reached by the use of different measurement techniques. The extensometer method is the most popular manner applied either in static or fatigue tests for strain components measurements versus time. This technique usually captures strain variations in a single direction defined at the beginning of experiment by the loading direction. The results collected in this way are important for typical engineering calculations carrying out in order to describe material behaviour in the uni-axial stress state conditions. For material examination under more complex loading, such data are insufficient, because many materials exhibit anisotropy of mechanical properties. Moreover, observations of damage zones and strain fields are not possible. Nowadays, the problems related to multiaxial stress/strain analysis may be effectively solved by the usage of modern, non-contact, optical methods, like DIC or ESPI for example.

DIC method, recommended for 3D measurements, is a stereoscopic technique that usually applies two CCD cameras, light sources and advanced software (GOM source). A mathematical description of DIC is available in the literature, Chu et al (1985) for example. The method requires an application of the special pattern represented by black dots on a grey background (Chu et al, 1985; Lord, 2009). Thanks to the markers defining the x, y and z coordinates, the method enables strain control up to the specimen fracture. DIC can use a pattern of rectangles or squares, that origins are directly selected for displacement/strain calculations. The results are presented in

the form of full-field maps expressing strain distribution from beginning of a test up to the specimen fracture (Chu et al, 1985; Lord, 2009). In further analyses the DIC maps can be compared with FEA results (Toussaint et al, 2008; Gower and Shaw, 2010; Kamaya and Kawakubo, 2011) in order to validate material models or constitutive equations. Digital Image Correlation is recommended for static and fatigue tests conducted under various programs of loading. In the case of static experiments, the DIC system is more flexible than in tests under cyclic loading. This is due to the limited number of stages offered by DIC software to be recorded. Therefore, a concept to capture strain variations due to cyclic loading should be formulated before testing by means of the software targets or commands in C++ code.

The results coming from various research groups show that DIC can be used for examination of material behaviour under typical tensile and compressive tests (Forster et al, 2012), fracture toughness examinations (Durif et al, 2012), and experiments for determination of the geometrical imperfection effects, such as notches and holes (Lord, 2009). Data of monotonic tensile tests are usually represented by the full-field maps reflecting strain distributions up to the fracture appearance. The results of fracture toughness experiments present strain distributions close to the fatigue crack, and enables the stress intensity factor values to be determined.

Electronic Speckle Pattern Interferometry is the second well known optical technique for displacement and strain measurements on the specimens surface. This noncontact and noninvasive technique is used in the fields of experimental mechanics to obtain the displacement maps during stress testing. It is a type of the holographic interferometry based on the analysis of laser beam, distracted from the optically rough surface. The image of the specimen due to the reflected laser waves is detected by the CCD (charge-coupled device) sensor of a camera and then transferred to a computer.

ESPI method is based on the application of the elementary wave phenomenon - interference. The interference process involves two beams: the first one illuminates the specimen surface, and as the reflected beam interferes with a second one - the reference beam. Through the subtraction process of the speckle interferograms (before and after loading up to the defined levels), correlation fringes are obtained. Having them, a phase map can be generated. It represents a distribution of displacement components in each direction, separately (Andersson, 2013). Final full-field stress and strain phase maps are created as the result of mathematical operations under the fixed boundary conditions (measurement area dimensions) and the material parameters (elastic modulus and Poisson's ratio). The usage of this method during fatigue testing enables the location of the greatest concentration of stress-induced defects and allows with high accuracy to predict the damage initiation. The presented method is a promising tool for identification of the real discontinuities such as defects and fractures.

6.2 Material Degradation Assessments Supported by Digital Image Correlation

6.2.1 Digital Image Correlation – Short Characterization of the Aramis 4M System

In majority practical cases, the DIC system is equipped with two digital cameras, Fig. 6.1. Usage of the single camera only enables obtaining also two-dimensional results, and moreover, for this type of configuration a time needed to achieve the final result is much shorter than in the case of a two-camera system, however, we do not have opportunity to capture the results in the third direction. The dimensions of the measurement area that can be analyzed using the Aramis 4M system cover a range from 10×7 [mm] to 4000×2900 [mm].

Regardless of a type of DIC system, single or double-cameras, a performance of the tests planned must be preceded by the calibration procedure of a device using the calibration plate containing the characteristic reference points, Fig. 6.1c. The object must be unloaded during calibration stage. In order to ensure validity of the calibration, it is necessary to provide coordinate values to the points visible in the middle area of the calibration plate. They must be greater than the coordinates of the remaining points. The whole process is based on the principle of correlation and the method of looking for points of the same coordinate values. The procedure requires a definition of the contour for analysis and registration of its shape, Fig. 6.1a. For this purpose, the characteristic points of the analyzed layer are assigned by square

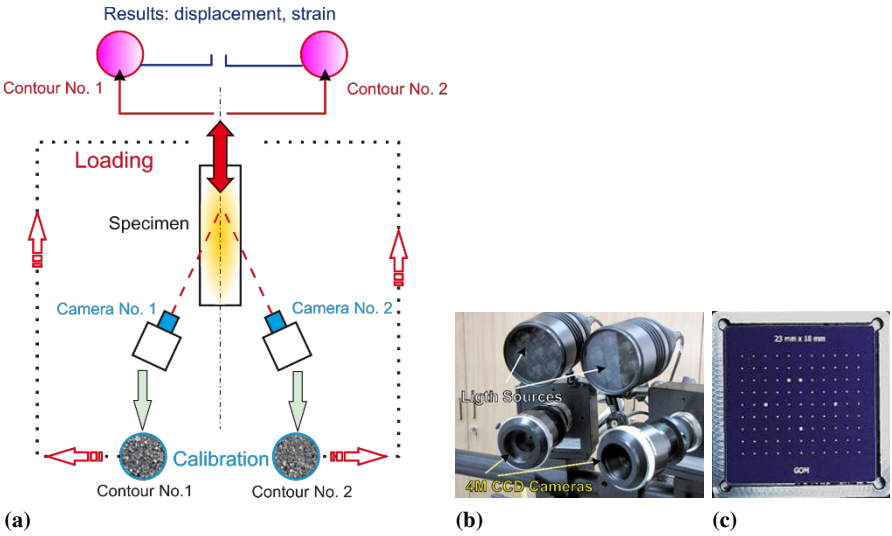

Fig. 6.1 ARAMIS system and its essential components: (a) general scheme of action (Toussaint et al, 2008), (b) main measurement module, (c) calibration plate

or rectangular areas (relatively small, e.g. 15 × 15 pixels) called "facets", Figs. 6.2 and 6.3.

Besides of the 15 × 15 pixel rectangular measurement areas, that can be changed in the DIC software, a segment of the gradient measuring zone is characterized by the presence of shared areas of the size of 2 × 2 pixels, Fig. 6.2. Into each of the rectangular areas a unique gray background with black points of any shape is assigned. It should be emphasized that in a research using DIC technique, it is necessary to select the shared zones. It should also be noted that sizes of "facets" affect the accuracy and speed of calculation. Increasing their dimensions decreases the accuracy of measurements, but on the other hand, it accelerates the time of the final result achievement. The rectangular areas are directly used in the analysis of displacement/strain components.

In the next stage the loading process is executed, during which the displacement components in the two- or three-dimensional area are determined. The values of displacement components are then used to calculate the strain/stress components in the form of full-field images. DIC system determines the coordinates in the two-dimensional (2D) system based on the reorientation of the rectangle/diamond centre of the facet, Fig. 6.3. The coordinates found using both cameras and the angle between their axes enable determination of the coordinates in the three-dimensional (3D) coordinate system. In the subsequent stages of analysis, a specific area of the layer with the gray-black background is identified. Its location can be used to find displacement. The initial stage (Stage 0) is assigned by the number "0", while the next stages by the subsequent numbers: "1", "2", "3", etc.

Difficulties occurring during DIC systems usage are mainly related to the preparation of the gray-black layer containing characteristic points located in the measuring zone of the specimen and the positioning of cameras, Fig. 6.1b, using a calibration plate, Fig. 6.1c.

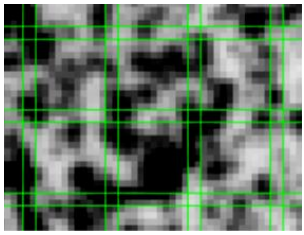

Fig. 6.2 A section of the measurement field with the facets arrangement defined by green lines (GOM, 2007)

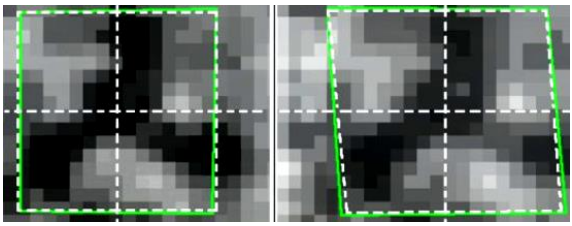

(a) (b)

Fig. 6.3 An example of an enlarged section of the analyzed area with a facet contour (green line) and a dashed line representing the relationship between the facets and strain: (a) before deformation, (b) after deformation (GOM, 2007)

DIC system designed for research in the field of large deformations can be successfully used to determine the Young's modulus, the Poisson's coefficient, and to identify the process of strengthening or weakening of the material in a wide range of plastic deformation. It is also applied in the study of materials with high ductility, exceeding 100%, and in determination of selected parameters of the fracture mechanics. In order to present high efficiency of DIC applications some representative results will be demonstrated in the next subsection.

6.2.2 Investigations of Material Behaviour Under Monotonic Tension Using Digital Image Correlation System

This section reports behaviour of engineering materials subjected to monotonic loading of specimen that had notches in the shape of "U" and "V". An influence of such geometrical imperfections on fatigue process is studied on the basis of the Wöhler diagrams, number of cycles to failure and fatigue notch factor. The results of experiments conducted by the use of Digital Image Correlation system called 4M Aramis are presented and discussed in detail. Tensile characteristic of the 41Cr4 steel, obtained by means of two independent techniques: standard extensometer and DIC, are compared. The experimental program provided the results that confirmed applicability of DIC technique for determination of typical mechanical properties. The equivalent full-field strain distributions are presented for specimens with and without the imperfections subjected to tension up to fracture. An influence of "U" and "V" notches on variations of tensile curve was evaluated.

6.2.2.1 Specimens with Notches

Notches are defined as geometrical imperfections of structural components. Their geometry is represented by the angle between their edges, radius and depth. Many results express values of stress concentration factor (SCF) obtained by analytical or numerical calculations. This enables the assessment of influence of stress concentration factor on stress values appeared in a notch tip. The second widely used method for determination of the SCF influence comes as a result of the development of Finite Element Analysis (FEA). In this case, advanced engineering software is used to solve problems caused by different kinds of geometrical discontinuities. In the case of this method many advantages can be stated, i.e. application of various 2D or 3D elements and analysis of macro- and micro-scales.

Its main drawbacks are material definition in the elastic-plastic state, as FEA requires definition of material hardening or softening reached not only in the uniaxial stress state, but also in a complex one. Despite of the use of modern, biaxial testing machines, the material examination under various combination of stress components is not easy and is still being under development.

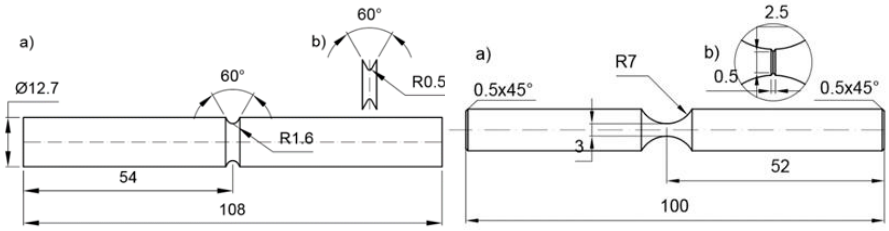

Fig. 6.4 Notched round specimens for fatigue testing (Fatemi et al, 2004; Pluvingae, 2001)

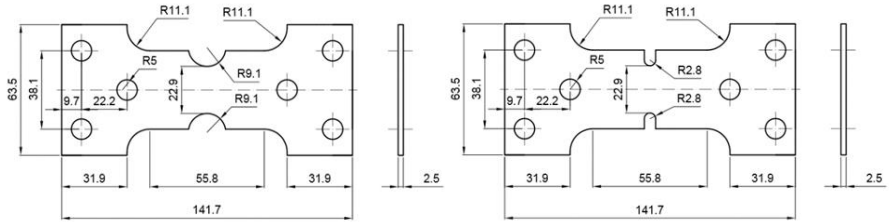

Fig. 6.5 Double-notched flat specimens used for examination of material behaviour under cyclic loading (Fatemi et al, 2004)

Notches can influence material behaviour and reduce the lifetime of components. They appear in drive shafts, engines, car bodies, turbines and others elements and constructions of complicated shapes. Among many features of notches, strongly related to their radius, angle, fillet at the tip, one can distinguish their size that can influence the concentration of stress/strain components, time to fracture and failure mode of the material.

Majority of specimens take a round or flat shape with macro- (Fig. 6.4) and micro-notches (Whaley, 1964; Maruno et al, 2003). The size of the geometric discontinuities is unique for each type of specimen, and depends on the details of the experimental procedure. In the case of round specimens, notches are machined around the major axis of the specimen (Figs. 6.4 and 6.5), but for flat specimens the geometric discontinuities are located on one (Whaley, 1964) or both sides of the specimen (Fig. 6.5).

6.2.2.2 Material Behaviour Affected by Notches and Holes – Previous Achievements

Essential efforts of many research groups (Wahl and Beuwkes Jr., 1930; Mazdumar and Lawrence Jr., 1981; Lanning et al, 1999; Milke et al, 2000; Fatemi et al, 2002, 2004; da Silva et al, 2012) are made to describe phenomenology of the influence of notches on material behaviour under various loading types up to fracture. As

mentioned previously, notched specimens are usually designed by individual projects of research groups.

Experimental results from tests for determination of the influence of notches on fatigue show their significant effect on lifetime (Figs. 6.6-6.8). The differences in lifetimes due to various stress levels can be even equal to 80% (Fig. 6.8). Boronski (2007) assumed that the fatigue life determined at the notch bottom is the same as the life for a smooth specimen when strains waveforms for the both specimens type are the same.

The results presented in Fig. 6.7 illustrate variations of the fatigue notch factor for values of the stress ratio R within a range of 0.5÷1.0, due to the radius of the notch machined in cylindrical and flat specimens. In the case of flat specimens, an increase of this parameter is clearly visible. For the cylindrical specimen, the value of the fatigue notch factor achieved a constant level.

Experimental procedures are also designed to elaborate the Wöhler diagrams on the basis of the stress controlled tests, applying notches with different values of the stress concentration factor (Fig. 6.8). These investigations are usually carried out using round or flat specimens. As can be seen in the papers by Fatemi et al (2002, 2004), a great decrease of the cycle number to failure was achieved when the SCF increased three times. Distribution of experimental points from tests performed on flat specimens, with the notch corresponding to the stress concentration factor equal to 1.787, exhibited low agreement in comparison to the approximation by semi-logarithmic function. The reason of such disagreement is usually related to the specimens machining process and their mounting in the testing machines.

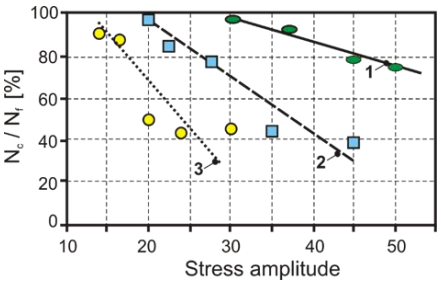

Fig. 6.6 Influence of notch radius on the proportion of cycle numbers to the initiation of the first crack (Nc) and fracture (Nf) at various stress amplitudes for the specimens: un-notched (1), notched with radius 1.5 mm (2); 6.35 mm (3); material: 24S-T4 aluminium alloy (Bennett and Weinberg, 1954)

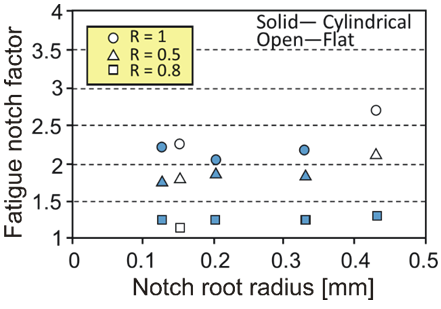

Fig. 6.7 Fatigue notch factor versus notch root radius for cylindrical and flat specimens with notches at a stress ratio within a range from 0.5 to 1; material used: Ti-6Al-4V (Lanning et al, 1999)

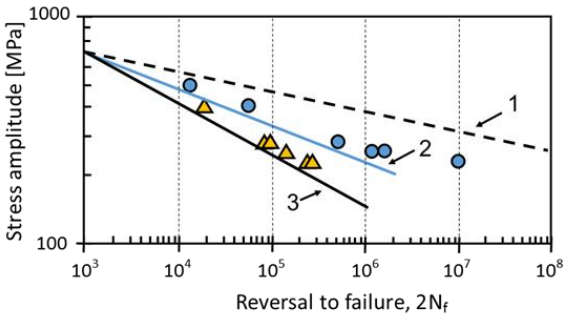

Fig. 6.8 Wöhler diagrams determined on the circumferentially notched round bars at stress concentration factors equal of 1.0 (1), 1.787 (2), 2.833 (3). Material: 1141 medium carbon steel micro-alloyed with Vanadium (Fatemi et al, 2002, 2004)

Other experiments were conducted to determine the zone of cracks initiation during fatigue (Fig. 6.9). In that case, the stress signal was used to control the testing machine. Both smooth and notched specimen geometries were applied (Qian et al, 2010). The application of smooth specimens in tests carried out at various stress levels allowed the initiation and propagation of cracks from the surface to the subsurface. In the case of notched specimens, the cracks appeared on the surface only.

Analytical and numerical calculations were concentrated on determination of stress gradients in the tip of the notch (e.g. Siebel and Stieler, 1955; Peterson, 1959; Milke et al, 2000). Their magnitudes were calculated using an equation representing dimensions of notches (Siebel and Stieler, 1955; Peterson, 1959; Pilkey, 1997), Neuber's theory (Neuber, 1961; Topper et al, 1967; Filippini, 2000; Neuber, 2001), and proportion of the stresses and nominal stress in the notch (Peterson, 1959; DuQuensay et al, 1986).

In FEM analysis, the influence of notches was calculated for specimens with narrow geometrical discontinuities like "V" or "U" (Pluvingae, 2001; da Silva et al, 2012; Andersson, 2013). The maximum stress in the tip of a notch (da Silva et al, 2012; Andersson, 2013) and the stress concentration factor were also determined

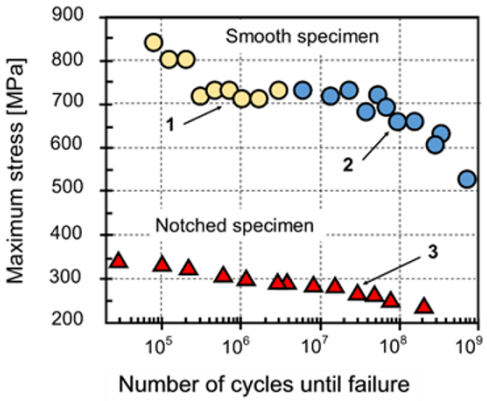

Fig. 6.9 Wöhler diagrams of the 40Cr steel, obtained for smooth and notched specimen with modes crack initiation: 1, 3 – surface; 2 – subsurface (Qian et al, 2010)

(da Silva et al, 2012) as well as an estimation of the fatigue strength (Andersson, 2013).

6.2.2.3 Material Behaviour Affected by Notches and Holes – Current own Achievements

Experimental procedure contained three stages:

1. determination of tensile characteristic;
2. investigation of the full-field strain distribution close to "U" and "V" notches;
3. examination of the influence of dimensions of "U" or "V" notches and their interactions on material behaviour.

All tests were carried out at room temperature using servohydraulic 8802 Instron and electro-dynamic Electropuls E10000 Instron testing machines. The Aramis 4M Digital Image Correlation system was applied to determine distribution of the strain components. Before testing, DIC device was calibrated. In the testing stages focused on determination of mechanical properties and material behaviour with the assistance of geometrical imperfections and various tensile rates, an extensometer and the 4M Aramis were used simultaneously. The assessment of DIC system used for determination of mechanical properties was made on the basis of a comparison of data obtained by the extensometer and by virtual tensometers defined in DIC software.

Application of Digital Image Correlation technique required the following stages:

1. adjustment of the distance between two cameras, its angle indicated in guidelines of technical data;
2. positioning the 4M Aramis with respect to the centre of the measurement zone;
3. selection of a calibration plate. that should be chosen on the basis of dimensions of the region for which the displacement is considered to be determined;
4. performing calibration procedure by application of the plate which takes various orientations in the 3D coordinate system, and recording its positions;
5. mounting the specimen, having an artificial measuring zone represented by black dots stochastically arranged on the grey layer, in grips of the testing machine;
6. capturing the first photo and establishing it as the reference one for displacement determination and strain calculations.

Technical data (GOM folders) for calibration of DIC system were delivered by the producer and contained the following features: measuring volume (height, length, width), minimum length camera support, distance ring (it enable to change a camera lens), measuring distance (from the central section of DIC device to the centre of the measuring zone), slider distance (determined by two technical points on the cameras), camera angle (it determines the centre of the measuring zone), calibration object (a plate with special regular markers having determined coordinates, which should be identified by cameras during the calibration process).

In the case of the experiments, the 4M Aramis was used at the following technical parameters:

- initial measuring zone determined on the specimen tested 25 × 10 × 3 [mm];
- calibration plate 25 × 18 [mm];
- slider distance 37.5 [mm];
- camera lens 75 mm + slider distance;
- camera angle 25°;
- sampling rate 2 photos/s.

Comparison of tensile curves obtained by the use of the flat specimen and the extensometer as well as DIC system is presented in Fig. 6.10. The axial stress was calculated as a proportion of the axial force to the cross-section of the measurement zone. Values of the axial strain were calculated for the same base.

Digital Image Correlation device and extensometer technique were simultaneously used in the monotonic test. For DIC calculations, two virtual tensometers were selected to define the gauge length for determination of the axial strain. A comparison of the results captured from the extensometer and DIC technique expressed a good agreement in the stress-strain curves from the beginning of testing up to the ultimate tensile strength occurrence. Differences in the last section of those characteristics are related to the appearance of neck, which was located close to the extensometer edge.

Mechanical properties calculated on the basis of data obtained by means of both techniques, are listed in Fig. 6.10. Differences between tensile characteristics are very small, indicating DIC system to be recommend not only for capturing strain maps (Fig. 6.11), but also for determination of typical mechanical parameters.

The main advantage of DIC system is presented in Fig. 6.11, which shows variations of the axial strain distribution at various stages of tension. On the basis of these results, the damage zone can be observed up to the specimen fracture (Fig. 6.11b-6.11d). It should be also mentioned that the distribution of the major strain (black vectors) at the beginning of tensile testing enables the assessment of specimen mounting quality in the testing machine (Fig. 6.11a).

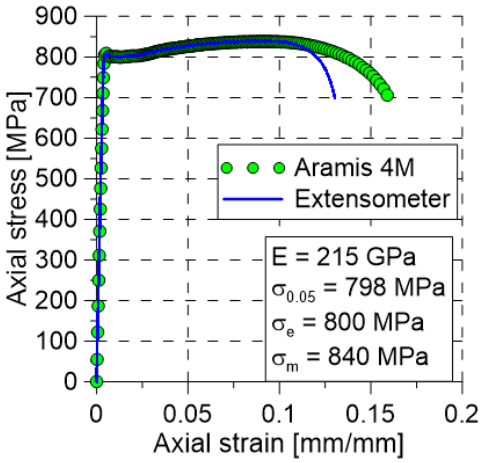

Fig. 6.10 Comparison of tensile characteristics determined by the use of the extensometer and the Aramis 4M. Material: high strength steel

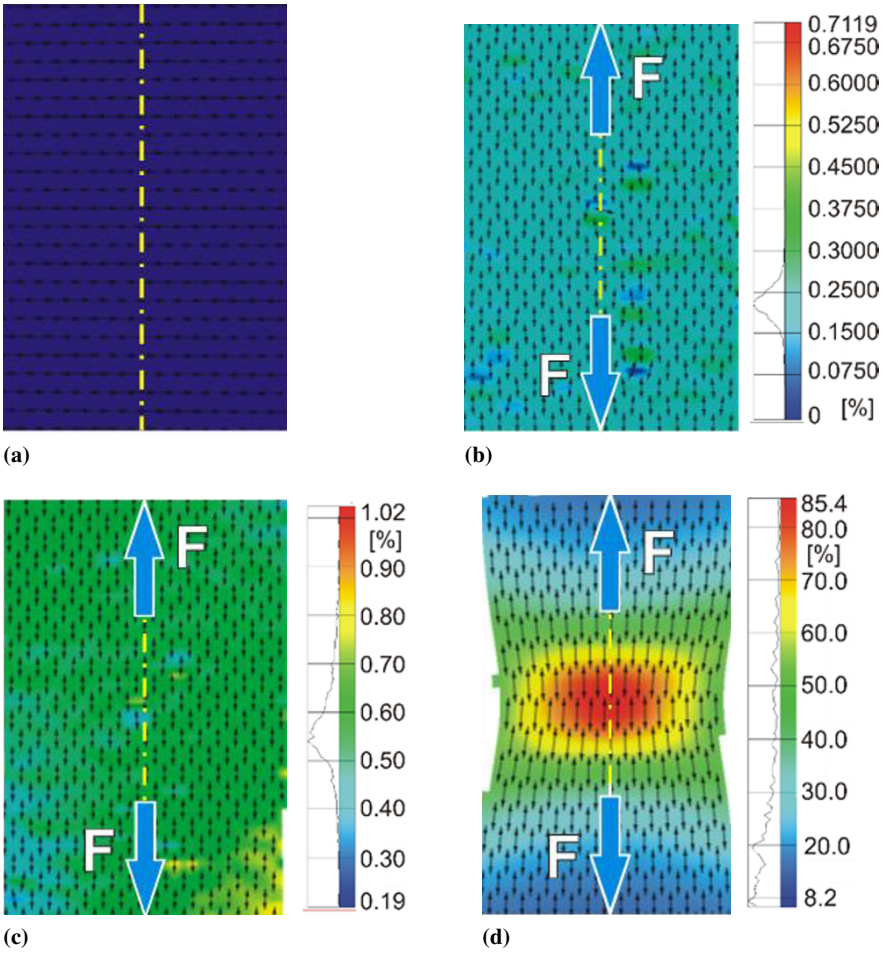

Fig. 6.11 Distribution of axial strain in the flat specimen under monotonic tension at various stages of the testing: (a) specimen mounted in the testing machine before the experiment; (b) stage corresponding to the proportional limit; (c) stage corresponding to the yield point; (d) stage before specimen fracture

Another application of DIC method is illustrated in Fig. 6.12. The subsequent images show the equivalent strain distributions for the specimen with the "U" - shaped notch at various material states. The 4M Aramis system calculates them using the following relationship:

$$\varepsilon_{\text{eq}} = \sqrt{\frac{2}{3}\left(\varepsilon^2_{1_{\text{true}}} + \varepsilon^2_{2_{\text{true}}} + \varepsilon^2_{3_{\text{true}}}\right)} \tag{6.1}$$

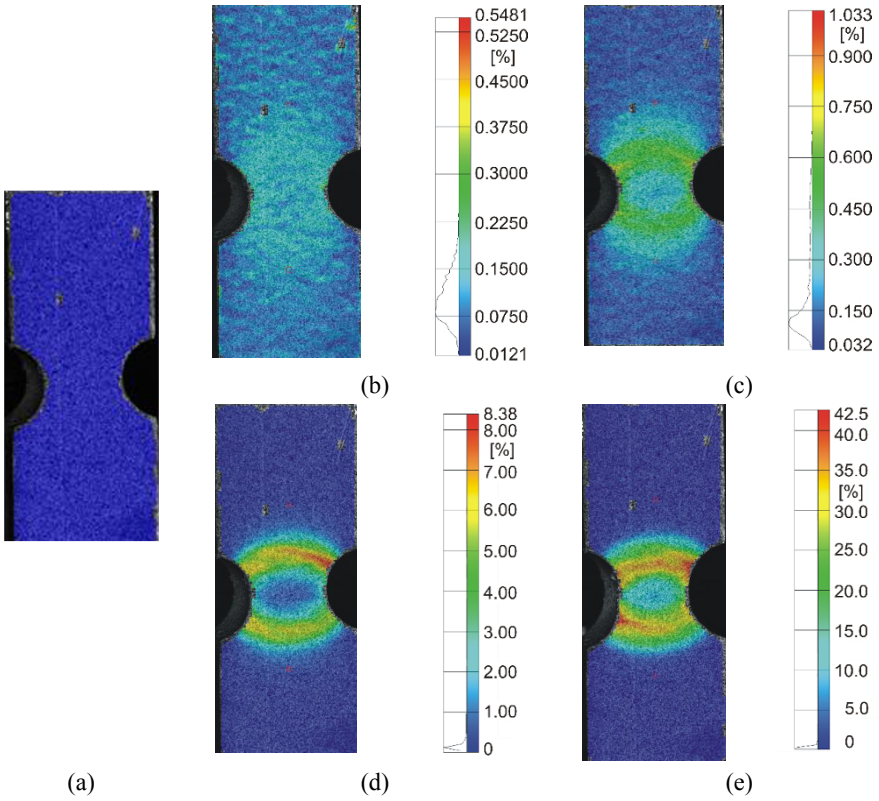

Fig. 6.12 The equivalent strain distribution in the "U"-notched specimen: (a) before loading, (b) elastic state, (c) initial phase of plastic state, (d) localization of damage, (e) damage development close to fracture. Material: aluminium

where: ε_i represents the major true strain components, $i = 1,2$ and 3. The major strain components are defined by the following equation

$$\varepsilon_{1_{\text{true}}} = \ln(1 + \varepsilon)$$

for which $\varepsilon = \Delta l / l_0$ is the engineering strain, where l_0 - gauge length, Δl - elongation. Equation (6.1) represents the stress state in the strain coordinate system. It can be found on the basis of theory of plasticity (Olszak, 1965; Chen, 2004; Westergaard, 2014). It should be emphasized that Eq. (6.1) can be used when the straining is proportional, i.e. the constant ratios of $d\varepsilon_{1_{\text{true}}} / d\varepsilon_{2_{\text{true}}} / d\varepsilon_{3_{\text{true}}}$ are fulfilled.

Both initial images show the specimen at the beginning of the test, i.e. the referential stage with zero loading and in the elastic state (Fig. 6.12a, b). The elastic-plastic state, shown in Fig. 6.12c, expresses the equivalent strain distribution and indicates the deformation zone located close to the centres of the "U"-notches being initiators of the maximum strain.

These arc-shaped deformation regions appear where the growing damage occurs. It is strongly evidenced in the following stages of specimen tension, presenting the material behaviour before fracture (Fig. 6.12d, e). As it can be noticed in Fig. 6.12c-e, the strain distribution is expressed by the zone in form of an arc at the test beginning up to the specimen fracture. It shows that besides of the strain concentration, which can be captured by DIC, the shape of strain fields should be taken into account as data for the further analysis of the effects related to "U"-shaped notch.

DIC system was also applied for determination of the influence of geometrical imperfection dimensions in form of the "U"-shaped (Figs. 6.13, 6.14) and "V"-shaped (Figs. 6.15, 6.16) on the material fracture. The depth of the notches was the same and equal to 1.3 mm. The radii of the "U"-notches were of 0.75 mm, 1.5 mm and 2.5 mm. The angles between the edges of the "V"-notches were expressed by: 10°, 60° and 90°.

Effects resulting from the dimensions of the "U" and "V" notches were determined based on variations of the equivalent strain isolines, Figs. 6.13, 6.15 (Szymczak, 2018). In the case of the "U" multi-notched specimen, the interaction between the notches became more significant with an increase of theirs radius (Fig. 6.13b). The results achieved for further tension also reflected this effect (Fig. 6.13c). It disappeared when the damage zone became greater (Fig. 6.13d). The cracks can also be followed on the basis of typical photos from the CCD cameras of DIC system (Fig.

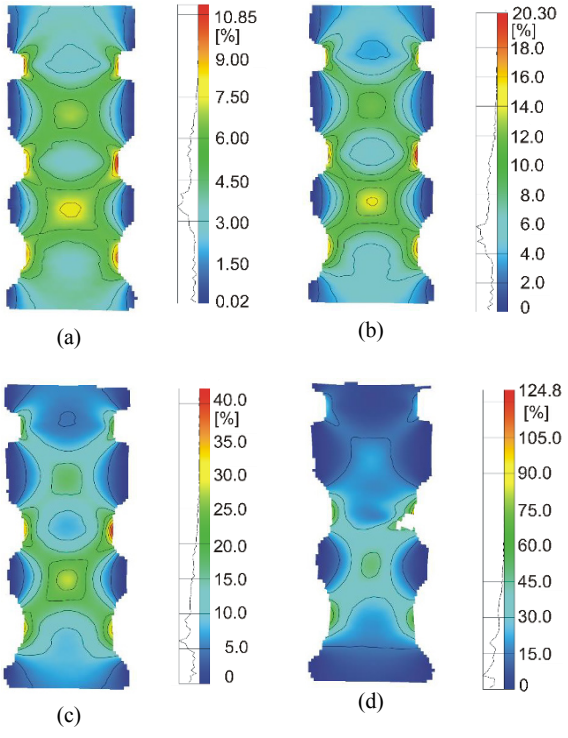

Fig. 6.13 The equivalent strain distribution in the U-shaped, multi-notched specimen at various stages of monotonic tension: (a), (b), (c) elastic-plastic state; (d) elastic-plastic state before fracture. Material: the 41Cr4 steel

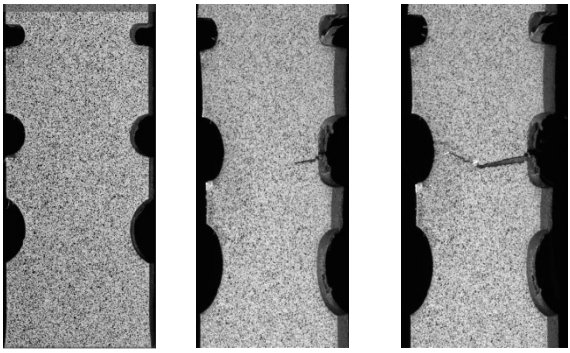

Fig. 6.14 The three stages of the "U"-notched specimen during monotonic tension: (a) before loading, (b) crack appearing, (c) crack growing

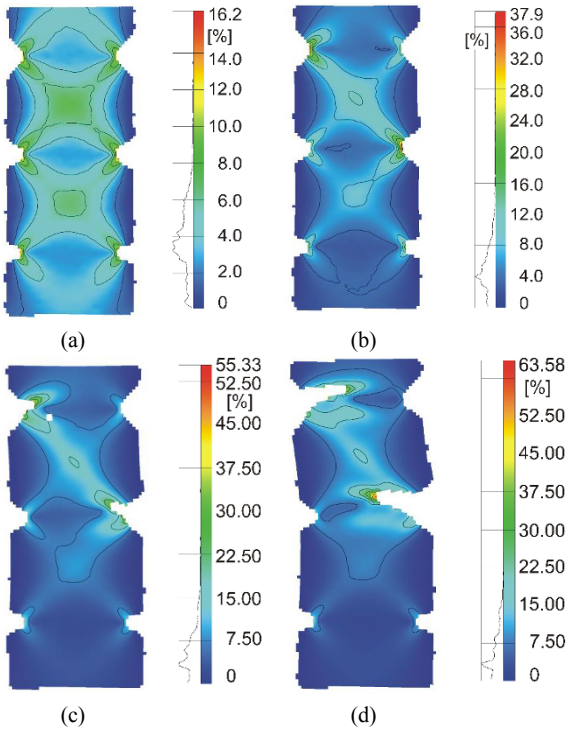

Fig. 6.15 The equivalent strain distribution in the multi-notched V specimen at various stages of monotonic tension: (a), (b) elastic-plastic state; (c), (d) elastic-plastic state before fracture. Material: the 41Cr4 steel

6.14). This is very important for the final stage of testing, because crack growing causes fracturing measurement pattern and, therefore, the digital correlation is not possible to be done (Figs. 6.13d, 6.14b, c).

Assessment of the effects of notches has been carried out using analytical equations for the stress concentration factor and the maximum stress (Pilkey, 1997). Their form for the multi-notched "U" specimens is noted in equation set (6.1), where: K_{tU} is the stress concentration factor, r is the notch radius, D - is specimen width, and L

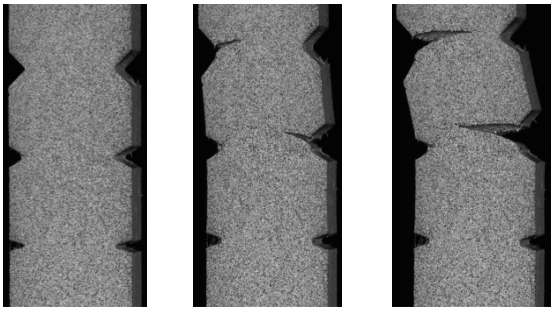

Fig. 6.16 The three stages of the "V" multi-notched specimen during monotonic tension: (a) before loading, (b) at crack initiation, (c) at crack growth

- is the distance between the notches, Fig. 6.17.

$$
\begin{aligned}
K_{tU} &= C_1 + C_2\left(\frac{2r}{L}\right) + C_3\left(\frac{2r}{L}\right)^2 + C_4\left(\frac{2r}{L}\right)^3,\\
C_1 &= 3.1055 - 3.4278\left(\frac{2r}{D}\right) + 0.8522\left(\frac{2r}{D}\right)^2,\\
C_2 &= -1.4370 - 10.5053\left(\frac{2r}{D}\right) - 8.7547\left(\frac{2r}{D}\right)^2 - 19.6237\left(\frac{2r}{D}\right)^3,\\
C_3 &= -1.6753 - 14.0851\left(\frac{2r}{D}\right) + 43.6575\left(\frac{2r}{D}\right)^2,\\
C_4 &= 1.7207 + 5.7974\left(\frac{2r}{D}\right) - 27.7463\left(\frac{2r}{D}\right)12 + 6.0444\left(\frac{2r}{D}\right)^3
\end{aligned}
\tag{6.2}
$$

Variations of the stress concentration factor versus notch radius expressed a linear reduction of its value with the radius increase, Fig. 6.18a. The same course was noticed for the maximum stress, as can be seen in Fig. 6.18a. This magnitude has been reached applying the following formula:

$$\sigma_{max} = K_{tU}\sigma_{nom} \tag{6.3}$$

where: $\sigma_{nom} = F/A_0$ – nominal stress, A_0 – area of specimen cross section for the measurement zone.

Looking at these results, it is easy to indicate the notches which are the dominant geometrical imperfections for the crack appearance, i.e. having a radius of 0.75 mm. This fact has not been confirmed by the DIC results in the final stage of tension (Fig.

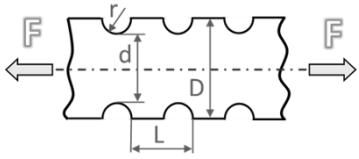

Fig. 6.17 "U" multi-notched specimen with the dimensions (Pilkey, 1997)

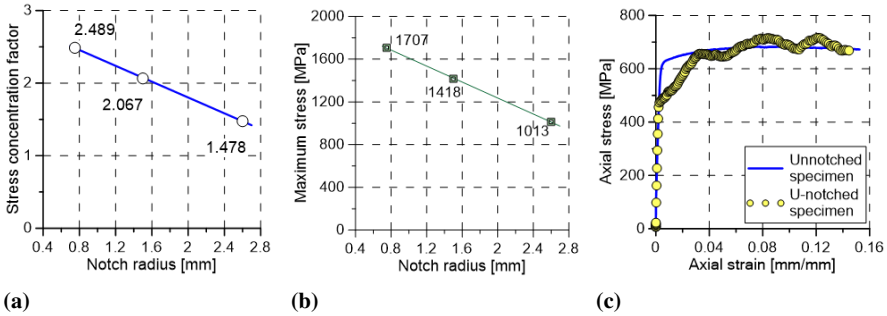

Fig. 6.18 The results for the multi-notched "U" specimen: (a) and (b) stress concentration factor and maximum stress as a function of notch radius, respectively; (c) tensile curve variations calculated by employing the cross section of the specimen

6.13), where the main crack occurred in the middle notch, for which the calculated maximum stress was lower (close to 300 MPa) than for the smallest one radius considered.

The effects resulting from the "V" notches presence can also be captured by means of DIC, Fig. 6.15 (Szymczak, 2018). For this type of geometrical imperfections, the full-field equivalent strain distributions close to the tip of the notches and the entire measurement section can be observed (Fig. 6.15b). Besides the different values of "V" notch angle, an indication of the main concentrator for the maximum strain is difficult. The 30° and 60° notches appear to have a very similar influence on the strain distribution at the beginning of the test. Further tension leads to an increase of the strain level in both notches located diagonally, which appear to be the main reason for initiation of damage zone (Fig. 6.15c). As a consequence, the equivalent strain increased, generating a fracture in the middle notch and then in the diagonal one (Fig. 6.15d).

For this type of geometrical imperfections, the stress concentration factor and the maximum stress have been calculated by the use of the following equation set (Pilkey, 1997):

$$\begin{aligned} K_{\mathrm{tV}} &= C_1 + C_2\sqrt{K_{\mathrm{tU}}} + C_3 K_{\mathrm{tU}}, \\ C_1 &= -10.01 + 0.1534\alpha - 0.000647\alpha^2, \\ C_2 &= 13.60 - 0.2140\alpha + 0.000973\alpha^2, \\ C_3 &= -3.781 + 0.07873\alpha - 0.000392\alpha^2, \end{aligned} \tag{6.4}$$

where, K_{tV}, K_{tU} are the stress concentration factors for the "V" and "U" notches, respectively; C_i are the coefficients, and α is the angle between the edges of the notches. The maximum stress has been found applying the following relationship

$$\sigma_{\max} = K_{\mathrm{tV}}\sigma_{\mathrm{nom}}$$

The results express a small lowering of the stress concentration factor and the maximum stress with decreasing of the notch angle, Fig. 6.19. These data well

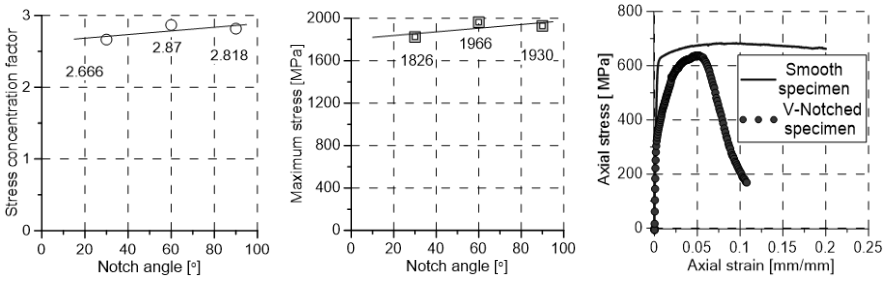

Fig. 6.19 The results for the "V" multi-notched specimen: (a) and (b) stress concentration factor and maximum stress as a function of notch angle, respectively, (c) tensile curve variations with respect to dimension of the cross section of the specimen

reflect the final stage of the multi-notched "V" specimen tension (Fig. 6.15d). Small differences between the values of the stress concentration factor and the maximum stress at various notch angles show that all of the "V" notches examined can also be treated as the potential places where the damage zones can occur.

The influence of the "V" notch on material straining during tension is illustrated in Fig. 6.19c presenting a comparison of tensile curves determined by the use of smooth and "V" multi-notched specimens. It is easy to notice that such geometrical imperfections caused the 50% reduction of elongation and 30% lowering of the yield point.

6.2.2.4 Damage Development Analysis Under Fatigue Conditions

Fatigue investigations were carried out on the MTS 810 testing machine, on plane specimens. These tests included specimens with three types of nickel alloy structure and with the layer thickness of 20 and 40 μm. Due to the continuous record of displacement maps, these tests were performed at high stress amplitude values equal to 600 MPa and 650 MPa, in order to reduce the test time to several hours. The loading frequency was 20 Hz, and the image was recorded every 5 seconds, i.e. the map was recorded every 100 cycles. Table 6.1 presents images from selected fatigue cycles obtained on a coarse grained specimen with a layer thickness of 20 μm. The amplitude of the alternating stress was 600 MPa. The specimen broke after 46 364 cycles, which is why the images recorded at the end of the specimen were compacted. For this specimen, the first signs of localization are visible after 45 thousands loading cycles. The increase in deformation at this stage is connected with the formation of a crack in the aluminide layer, which propagates into the material until the cohesion is entirely lost. On this basis, the moment of crack formation can be estimated, although the detection threshold is lower than that in the technically comparable ESPI method

Table 6.1 Images showing strain distribution maps captured by DIC

10 000 cycles	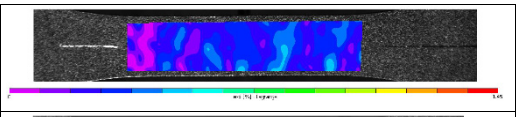
15 000 cycles	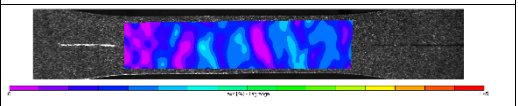
20 000 cycles	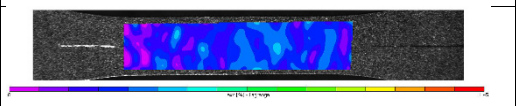
25 000 cycles	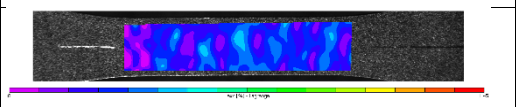
30 000 cycles	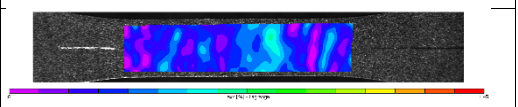
40 000 cycles	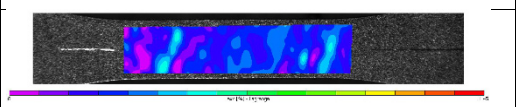
45 000 cycles	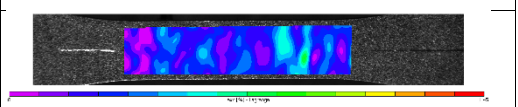
45 600 cycles	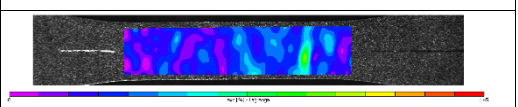
45 800 cycles	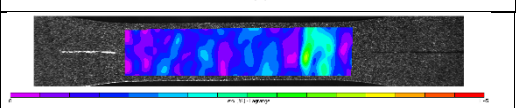
46 000 cycles	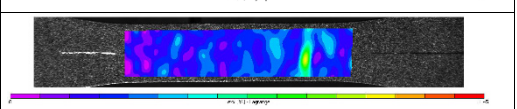
46 100 cycles	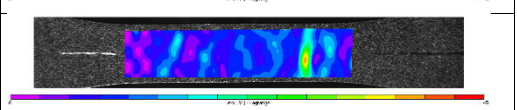
46 200 cycles	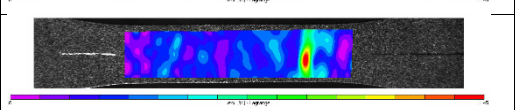
46 300 cycles	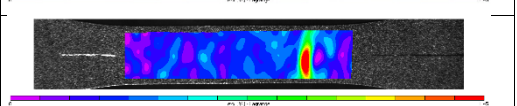

obtained. Subsequent images refer to the coarse specimen with the layer thickness of 40 μm.

6.2.2.5 Final Remarks Related to the Digital Image Correlation Technique Application

Digital Image Correlation method can be applied for tests on specimens with or without geometrical imperfections. It enables capturing damage zones up to the specimen fracture. The method identifies the interaction of strain fields resulting from the notches presence. The isolines created on the surface of multi-notched specimen appeared at the initial stage of tension and disappeared at the moment of damage zones creation and crack appearance. Independently on a type of geometrical imperfections considered, a significant reduction of proportional limit and yield point can be easily indicated. Typical DIC device is able to identify a strain distribution close to the notch for elastic-plastic state. In the case of elastic state, the micro-DIC method using microscope device is more recommended.

Thanks to the DIC technique such mechanical properties as the Young's modulus, yield point, ultimate tensile strength and elongation can be easily determined. More importantly, the technique with some limitations in the accuracy of strain measurement, can be attractive for damage development identification on surfaces and subsurfaces. It can be also used to monitor deformation changes at high-temperature fatigue tests, however, the usage of the induction heater reduces the field of the camera view significantly. Nevertheless, the application of DIC to analysis of the strain distribution changes seems to be a valuable tool for the monitoring of damage development on the surfaces of many responsible elements of structures and machines, including an identification of the places of the cracks initiation and their further propagation.

Due to limited accuracy of the method in terms of damage monitoring, especialy in early stages of the fatigue process development, Electronic Speckle Pattern Interferometry is regarded as more suitable for damage inspection. The main working principles of this technique together with some examples of application will be described in the next section.

6.3 Material Degradation Assessment Supported by Electronic Speckle Pattern Interferometery

6.3.1 Working Principles of Electronic Speckle Pattern Interferometery

Electronic Speckle Pattern Interferometry (ESPI) is the next powerful non-destructive optical method of stress and strain monitoring for early detection, localization and

monitoring of damage in materials under monotonic and cyclic loading (Vial-Edwards et al, 2001; Patorski, 2005; Gungor, 2009; Pierron, 2009; Dietrich et al, 2012; Szymczak et al, 2013; DANTEC, 2019). ESPI method allows to monitor a deformation development until the specimen decohesion. A typical measuring system consists of the CCD camera localized in the head of the system and four light sources (Fig. 6.20). A reference speckle pattern formed by the reference beam is also observed by the camera. The typical light source used in ESPI is a 75-mW Nd: YAG laser, emitting a green beam with the wave length of λ=785 nm. It is divided by the beam-splitter into four beams. The image of the specimen due to the reflected laser waves is detected by a CCD (charge-coupled device) sensor of the camera and then transferred to the computer.

The results obtained by means of ESPI are derived from the physical surface deformations. This noncontact and noninvasive technique is used in experimental mechanics to obtain the displacement maps during the loading process. ESPI is based on the application of the wave interference phenomenon. The main purpose of this method is to obtain the fringe patterns which represent waves interference from the coherent light sources illuminating surface of the object. The electromagnetic waves are superimposed and the resulting wave intensity pattern is determined by the phase difference between the waves. The illumination of a rough surface with coherent laser light and subsequent imaging using a CCD camera generates statistical interference patterns, the so-called speckles. These speckles are inherent to the investigated surface. Superimposing a reference light, which is split out of the same laser source, on these speckles results in an interferogram. If the object under test is loaded, and the surface is deformed, the speckle interferogram changes. Comparing an interferogram of the surface before and after loading will result in a fringe pattern, which reveals the displacement of the surface during loading as contour lines of deformation.

As shown in Fig. 6.21, the laser beam is divided into an object beam (blue line) and reference beam (green line). When the object is displaced in the direction normal to the viewing direction, a distance travelled by the object beam changes, and as a consequence, the amplitude of the combined beams becomes altered. The speckle effect is a result of the interference of waves having different amplitudes (Fig. 6.22). This process can be analysed mathematically. Let us consider a pair of

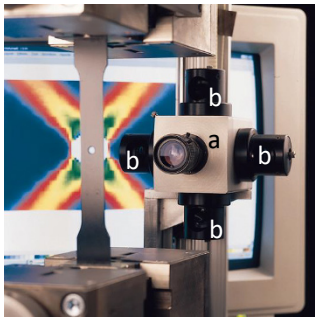

Fig. 6.20 ESPI system: (a) CCD camera, (b) light sources (DANTEC, 2019)

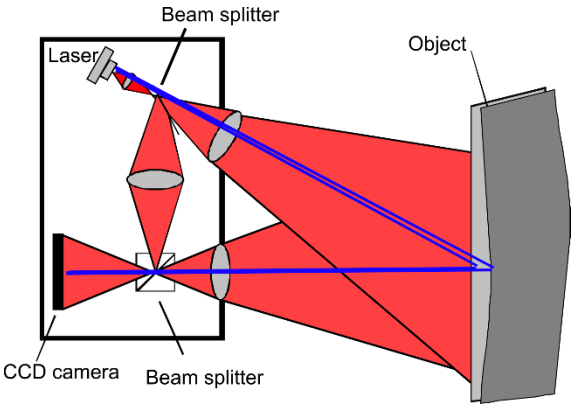

Fig. 6.21 Laser speckle interferometry set-up (DANTEC, 2019)

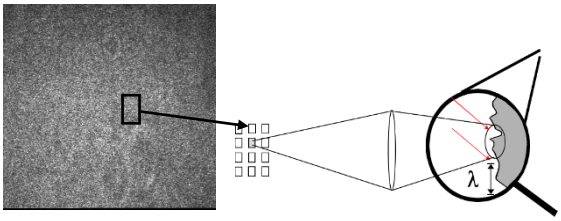

Fig. 6.22 Origin of the speckle (DANTEC, 2019)

simple coherent waves expressed by:

$$\begin{aligned} U_1(x,y) &= A_1 \mathrm{e}^{-\mathrm{i}(\omega t - \varphi_1(x,y))} \\ U_2(x,y) &= A_2 \mathrm{e}^{-\mathrm{i}(\omega t - \varphi_2(x,y))} \end{aligned} \tag{6.5}$$

where (x, y) represent the coordinates of the image plane, A is the magnitude of the displacement, $\varphi(x, y) = \varphi_1(x, y) - \varphi_2(x, y)$ represents the phase difference between the two beams, and ω denotes the angular frequency. The light wave intensity can be found using the following equation:

$$I(x,y) = \int [U_1(x,y) + U_2(x,y)][U_1^*(x,y) + U_2^*(x,y)]dt \tag{6.6}$$

Applying Eqs. (6.5), the intensity of the light wave expressed by Eq. (6.6) can be transformed into the following relationship:

$$\begin{aligned} I(x,y) &= A_1^2 + A_2^2 + 2A_1A_2\cos[\varphi_1(x,y) - \varphi_2(x,y)] \\ &= A_1^2 + A_2^2 + 2A_1A_2\cos[\varphi(x,y)] \end{aligned} \tag{6.7}$$

Thus, the amplitude of the light at any point of the image is the sum of the light amplitude of the reflected wave from the object and that which represents reference beam.

The speckle effect occurs when the rough surface is illuminated by the coherent light, if the surface roughness is greater than the wavelength λ. As the result of the light beam scattering on the object surface, the interference of secondary waves occurs, which leads to the formation of the characteristic speckle pattern.

When the specimen is deformed, the speckle pattern obtained before loading (reference image) is subtracted from the speckle pattern obtained after loading (measurement image), fringes are obtained which represent contours of displacement (see Fig. 6.23). The fringes represent the points of the same displacement. Based on the fringe image, it is not possible to find a direction of displacement.

The intensity distributions $I_1(x, y)$ and $I_2(x, y)$ recorded before and after the object displacement can be expressed by the following equations:

$$I_1(x, y) = A_1^2 + A_2^2 + 2A_1A_2 \cos[\varphi(x, y)] \tag{6.8}$$

$$I_2(x, y) = A_1^2 + A_2^2 + 2A_1A_2 \cos[\varphi(x, y) + \Delta\varphi(x, y)] \tag{6.9}$$

where $\Delta\varphi(x, y)$ is the additional phase change due to the object deformation (Fig. 6.24). Figure 6.24 shows that bright interference bands (containing the maximum intensity values) occur in places where the phase difference is of the even multiple of π. Dark bands (containing the minimum values of intensity) correspond to phase difference of the odd multiple of π. A new interference fringes are obtained by subtracting the signals:

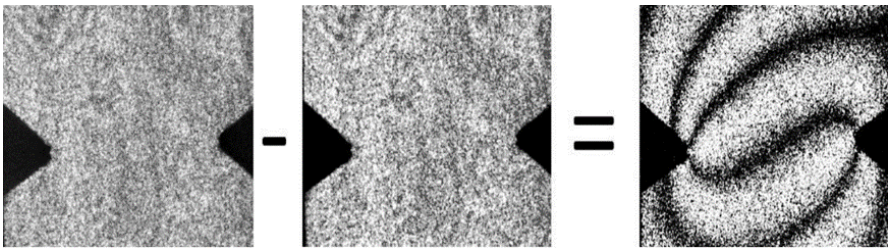

Fig. 6.23 A schema of the fringe patterns determination (DANTEC, 2019)

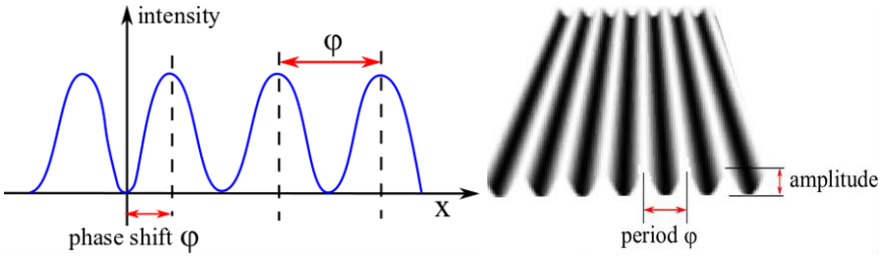

Fig. 6.24 Original sinusoidal signal

$$I(x,y)_{\text{after}} - I(x,y)_{\text{before}} = 2A_1A_2\{\cos[\varphi(x,y) + \Delta\varphi(x,y)] - \cos[\varphi(x,y)]\} \quad (6.10)$$

In the case of adding the signals of the wave intensity one can obtain

$$I(x,y)_{\text{after}} + I(x,y)_{\text{before}} = 2A_1^2 + 2A_2^2 + 2A_1A_2\{\cos[\varphi(x,y) + \Delta\varphi(x,y)] + \cos[\varphi(x,y)]\} \quad (6.11)$$

The intensity of the interference pattern takes the form:

$$I_j(x,y) = A_1^2 + A_2^2 + 2A_1A_2\cos[\varphi(x,y) + \alpha_j] \quad (6.12)$$

where α_j is the amount of phase shifting with $j = 1,2,3,\ldots,N$ representing the integer number depending on the phase shifts number introduced. Applying the four-phase shift method $(-3\pi/4, -\pi/4, \pi/4, 3\pi/4)$, the phase of the wavefront computed from the four interferograms is

$$\varphi(x,y) = \arctan\frac{I_4(x,y) - I_2(x,y)}{I_1(x,y) - I_3(x,y)} \quad (6.13)$$

There are three unknown values: $A_1, A_2, \varphi(x,y)$ and α_j is a known optical phase shift. With the intensity maps the optical phase at each pixel can be calculated. Minimum three images with different relative optical path length are acquired. Finally, one can calculate the optical phase for each deformation stage (Fig. 6.25). A difference between the phase maps calculated after and before the deformation is given by

$$\Delta\varphi(x,y) \equiv \varphi(x,y)^{\text{after}} - \varphi(x,y)^{\text{before}} \quad (6.14)$$

On the other hand, the optical path difference (OPD) for the object wavefront relative to the reference wavefront can be determined from:

$$\text{OPD}(x,y) = \frac{\lambda\Delta\varphi(x,y)}{2\pi} \quad (6.15)$$

The OPD is related to surface heights by the multiplicative factor and accounts for illumination angles and viewing which may differ from the normal surface.

Therefore, the phase change

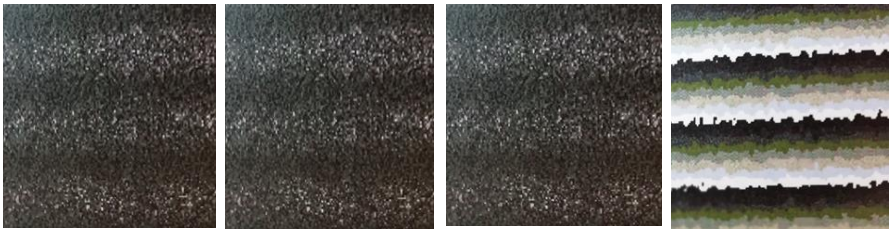

I_1 I_2 I_3 φ

Fig. 6.25 Phase shift algorithm (DANTEC, 2019)

$$\Delta\varphi(x,y) \equiv \varphi(x,y)^{\text{after}} - \varphi(x,y)^{\text{before}}$$

of the wavefront from the object surface before and after deformation is directly associated with the component of displacement $u(x)$ and can be expressed as

$$\Delta\varphi(x,y) = \frac{4\pi}{\lambda} \sin\theta u(x,y) \tag{6.16}$$

where λ is the length of laser wave, and θ is the incident angle between two light beams illuminating the object, and $u(x)$ is the in-plan displacement component.

Finally, one can calculate the optical phase for each deformation stage (Fig. 6.26a). The next point is to unwrap the phase map. A definition of the starting point is required (see Fig. 6.26a). The offset $(n * 2\pi)$ must be taken into account. The displacement is encoded as levels of gray that represent the intensity at a given pixel $I(x,y)$ of the scalar field. Finally, the continuous phase map is determined, Fig. 6.26b.

In the next step the strain is calculated. Determination of the fringe pattern gradient is shown in Fig. 6.27. Taking into account Fig. 6.27, the following relationship can be formulated:

$$\tan\theta_u = \frac{\dfrac{\partial u}{\partial y}}{\dfrac{\partial u}{\partial x}} \tag{6.17}$$

Applying the relationship between the derivative of displacement components and the fringe orientation of the object before and after deformation, the strain components can be found according to the following equations

$$\frac{\partial u}{\partial x} = \varepsilon_{xx}, \quad \frac{\partial u}{\partial y} = \gamma_{xy}, \quad \frac{\partial v}{\partial x} = \gamma_{yx}, \quad \frac{\partial v}{\partial y} = \varepsilon_{yy} \tag{6.18}$$

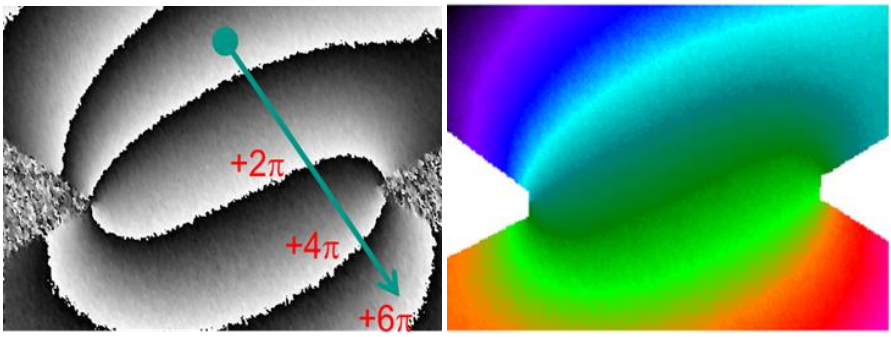

(a) **(b)**

Fig. 6.26 Elaboration of ESPI measurements: (a) Phase map, (b) Continuous phase map (DANTEC, 2019)

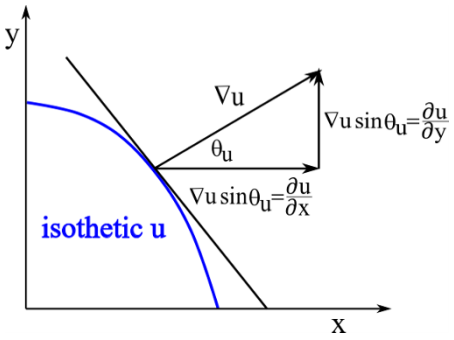

Fig. 6.27 Gradient vector and the partial derivatives with respect to the coordinate axes

The principal strain components are defined by the formulas

$$\varepsilon_{h_1} = \frac{\varepsilon_{t_1} + \varepsilon_{t_2}}{2} + \sqrt{\left(\frac{\varepsilon_{t_1} - \varepsilon_{t_2}}{2}\right)^2 + \left(\frac{\gamma_{t_1 t_2}}{2}\right)^2},$$
$$\varepsilon_{h_2} = \frac{\varepsilon_{t_1} + \varepsilon_{t_2}}{2} - \sqrt{\left(\frac{\varepsilon_{t_1} - \varepsilon_{t_2}}{2}\right)^2 + \left(\frac{\gamma_{t_1 t_2}}{2}\right)^2} \tag{6.19}$$

ESPI is implemented by producing interference between an optical wavefront scattered from the object and the fixed reference wave, giving as a consequence the displacement components for each point in the image of the object. The use of this method during fatigue testing enables the location of the greatest concentration of stress-induced defects to be determined, and more importantly it provides necessary data for damage initiation predictions with relatively high accuracy. This issue will be wider presented in the next subsection.

6.3.2 Representative Applications of Electronic Speckle Pattern Interferometry in the Laboratory Investigations

6.3.2.1 The Results for the Nickel Alloy

Fatigue investigations were carried out on nickel alloy (C – 0.09%, Cr – 8.8%, Mn – 0.1%, Si– 0.25%, W– 9.7%, Co – 9.5%, Al – 5.7%, Ta+Ti+HF– 5.5%) under force control using the MTS-810 hydraulic testing machine. In each test the maximum cyclic stress range and stress amplitude were equal to 600 MPa and 300 MPa, respectively. Both these parameters were lower than the yield point of the material in question. In order to eliminate vibrations of the testing machine during optical measurements the loading process of the specimen was executed manually using a special device designed originally by the IPPT PAN workers. The loading programme is presented in Fig. 6.28.

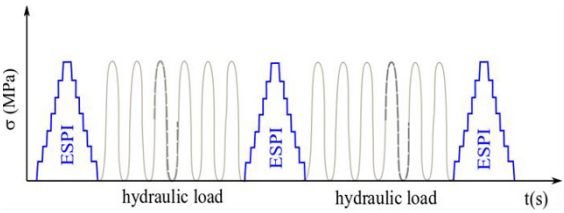

Fig. 6.28 Scheme of loading during fatigue test

As it is shown, the first cycle was conducted manually, and subsequently, a block of cycles under the frequency of 10 Hz was carried out using the testing machine (Kopeć et al, 2012). The process of cyclic loading was interrupted several times in order to perform displacement measurements by means of the ESPI camera. The experimental programme provided displacement measurements at the beginning of test and after 20000, 40000 and 50000 cycles. The number of cycles to failure was $N_f = 54315$.

ESPI observations carrying out at various stages of the fatigue degradation represent a status and dynamics of the damage development. They enable a determination of the areas of the greatest stress concentrations and reflect a local character of the fatigue damage initiation.

The field strain distributions along the Y axis corresponding to the acting stress direction in the specimen are presented in Fig. 6.29. The figure shows strain distributions for different stages of the fatigue process, i.e. after: (a) first cycle; and (b) 50000 cycles. It has to be mentioned, that all these maps were obtained for the same scale in order to enable a direct comparison of the results achieved. As it is seen, the method enables identification of places where damage initiates. Figure 6.30 demonstrates a location of decohesion on the specimen gauge length, that well agrees with the largest displacement concentration occurring on the phase maps captured by means of the ESPI measurements.

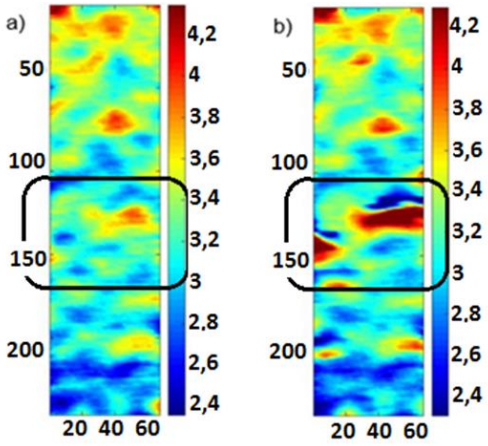

Fig. 6.29 The field strain distribution along Y axis corresponding to the acting stress direction. Measurements performed: (a) in the first loading cycle; (b) after 50000 cycles. Scale is matched to the extreme strain values in the first measurement

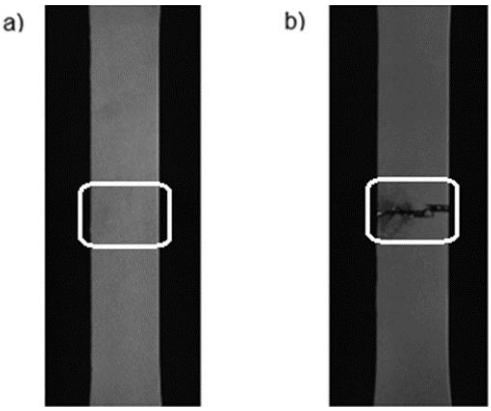

Fig. 6.30 Fatigue specimen photo: (a) before the test; (b) after the test (N_f = 54315 cycle)

In Fig. 6.31 another example of the strain distribution map obtained using ESPI for nickel alloy is presented for increasing number of loading cycles. The lateral profiles of maximal cross-sectional strain distribution for increasing cycles number are presented in Fig. 6.32. They enable identification of the highest values of strain on the strain distribution maps, and therefore, provide info for the indication of potential places of damage initiation.

6.3.2.2 The Results for the P91 Steel

The specimens used in this study were manufactured using X10CrMoVNb9-1 (P91) polycrystalline steel. This is a low carbon, creep-resistant steel, typically used for

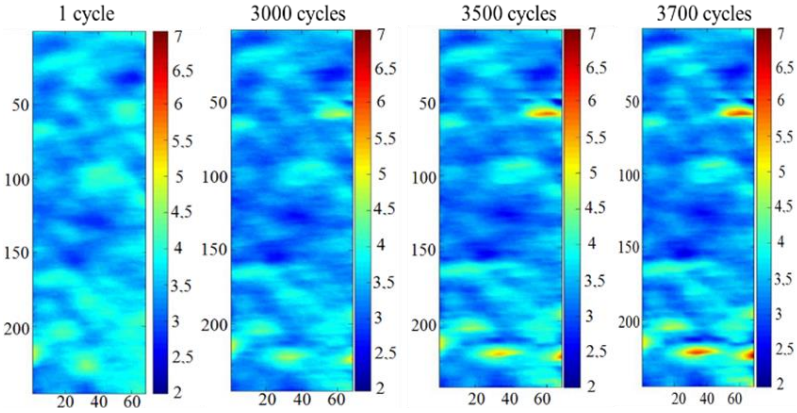

Fig. 6.31 Strain distribution map on the plane specimen surface using ESPI for different stages of the fatigue process

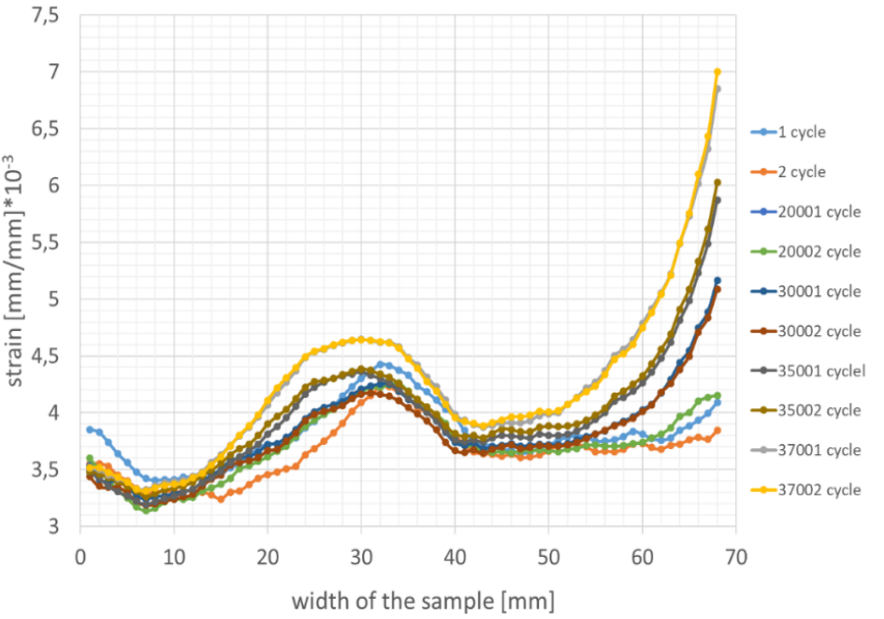

Fig. 6.32 The lateral profiles of the maximal cross-sectional strain evolution

tubes, plates and structural components in the power plant industry. The content of alloying elements in P91 is given in Table 6.2.

Table 6.2 Chemical composition of the P91 steel (in wt. %)

Element	C	Mn	Cr	Mo	V	Ni	Cu	Si	S
P91	0,2÷0,5	0,3÷0,6	8÷9,5	0,85÷ 1,1	0,18÷0,25	< 0,4	< 0,3	0,08÷0,12	< 0,01

The purpose of tests on P91 steel was to provide experimental data of the evolution of micro-strain regime during high cycle fatigue crack initiation. The whole fatigue process was divided on the blocks of cycles and carried out using the hydraulic servocontrolled testing machine. The process of cyclic loading was interrupted several times after selected numbers of cycles in order to perform displacement measurements by means of the ESPI camera. Strain distribution maps at the maximum load applied on the plane specimen surface using ESPI are presented for increasing number of the loading cycles in Figs. 6.33, 6.34 and 6.35. Three types of specimens were tested: specimen with relatively rough surface, electropolished specimen and specimen with the hole. The different stages of the fatigue process, from the beginning up to the moment of crack initiation and subsequent propagation are presented.

During the process of cyclic loading the material deforms heterogeneously and numerous strain concentration spots are visible in the case of rough specimen, Fig.

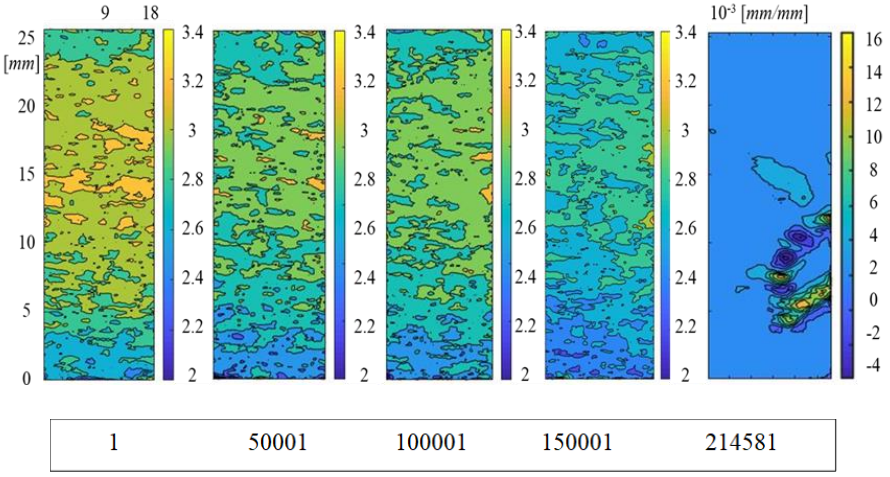

(a)

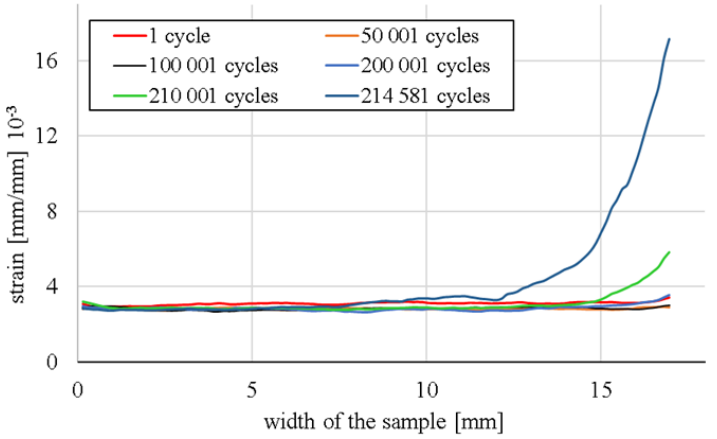

(b)

Fig. 6.33 The lateral profiles of the maximal cross-sectional strain evolution

6.33a. The lateral profiles of the maximal cross-sectional strain distribution for increasing cycles number for rough specimen on the surface are presented in Fig. 6.33a. It is expected that the microstructure of the material plays an important role in the strain localization. In order to reduce roughness and remove some modification of the material properties resulting from electro-machining (local heating-cooling), the surface of specimen was electro-polished in the vicinity of cracks generated in the fatigue process.

The strain distribution maps are presented in Fig. 6.34a. The lateral profiles of the maximal cross-sectional strain distribution for increasing cycles number for

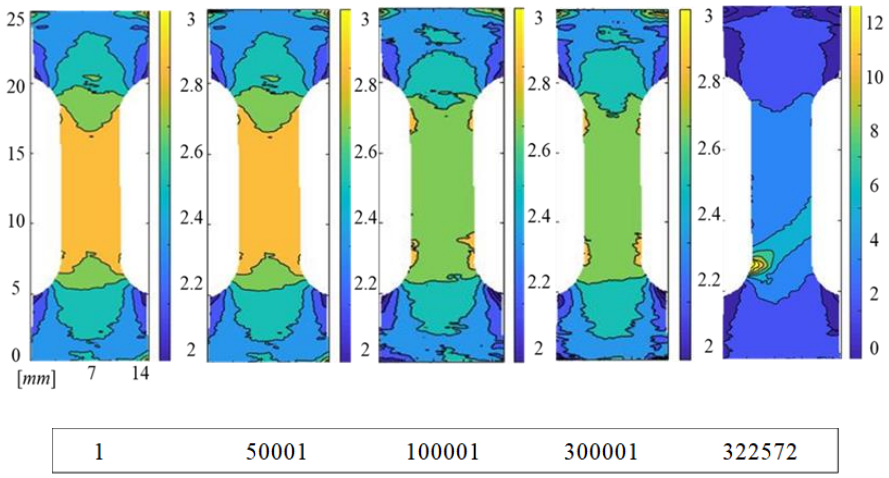

(a)

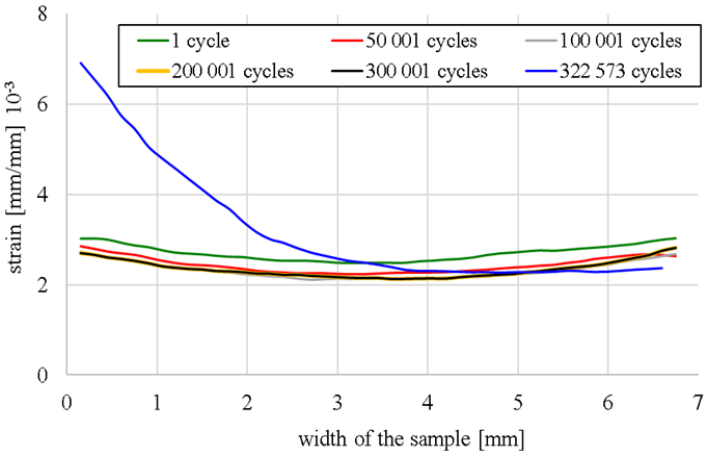

(b)

Fig. 6.34 The lateral profiles of the maximal cross-sectional strain evolution

electropolished specimen are presented in Fig. 6.34b. As it is seen from the profiles, Figs. 6.33b and 6.34b, the places of damage initiation are simple for identification. They are well represented by the significant increase of strain.

In the case of specimen with the hole, in the first cycle the strain accumulation spot is visible near the hole, (Fig. 6.35, 1 cycle). In the next cycles the material is strengthened (Fig. 6.35, 2 cycles), but the local zones of strain accumulation in the vicinity of the hole can be still observed, however, they have slightly lower level in comparison to the first cycle. The crack localisation on the left side of the hole is presented in Fig. 6.35 after 78057 cycles.

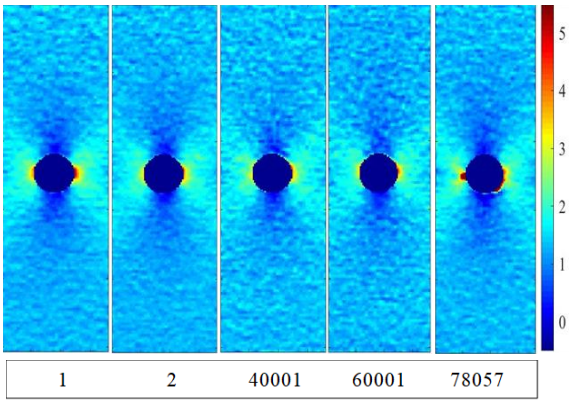

Fig. 6.35 Strain distribution maps - specimen with the hole

6.3.2.3 Mathematical Modelling of Fatigue Damage Evolution, Numerical Implementation Supported by Electronic Speckle Pattern Interferometry Results (Ustrzycka et al, 2017)

In this section the mathematical description of fatigue crack initiation and evolution is formulated. The problem of damage evolution for metals subjected to cyclic loading inducing fatigue crack initiation and its propagation within the elastic regime is considered. The condition of damage accumulation is formulated after Mróz et al (2005). It is assumed that, when the critical stress condition is reached on the material plane, the damage zone Ω is generated. Afterwards, the growth of damage zone can be described. The mathematical model is applied to study damage evolution under cyclic tension and the predictions are compared with experimental data. The profile of normal strain $\varepsilon(x)$ and stress $\sigma(x)$ along the damage zone Ω is expressed as a sum of mean $(\bar{\varepsilon}, \bar{\sigma})$ and fluctuation $(\tilde{\varepsilon}(x), \tilde{\sigma}(x))$ components

$$\varepsilon(x) = \bar{\varepsilon} + \tilde{\varepsilon}(x), \qquad \sigma(x) = \bar{\sigma} + \tilde{\sigma}(x) \tag{6.20}$$

The material is assumed to be linearly elastic, but exhibiting a damage process at strain concentration zones. In order to illustrate the problem (Fig. 6.36), a potential damage zone Ω is selected with the largest strain and stress fluctuations.

The damage evolution rule (6.21) was originally formulated by Mróz et al (2005) for brittle materials

$$dD = A\left(\frac{\sigma - \sigma_0^*}{\sigma_c - \sigma_0}\right)^n \frac{d\sigma}{\sigma_c^* - \sigma_0^*} \tag{6.21}$$

where A and n denote material parameters, σ_0 is the damage initiation threshold values, σ_c denotes the failure stress in tension for the damaged material, σ_0^* and σ_c^* are the threshold values for the undamaged material and D denotes the scalar measure of damage ($0 \le D \le 1$).

The stress value σ increases but the values of σ_0 and σ_c decrease. Both σ_0 and σ_c depend on the damage state according to the formula

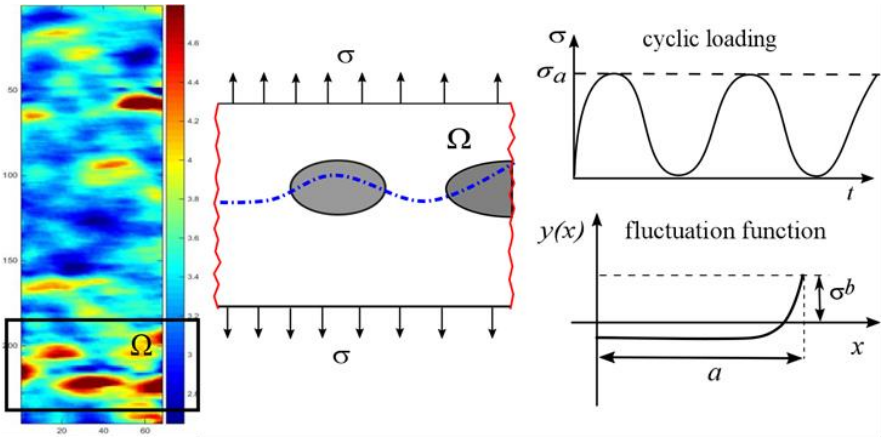

Fig. 6.36 Damage zone Ω with the major stress fluctuation

$$\sigma_{\mathrm{c}} - \sigma_0 = (\sigma_{\mathrm{c}}^* - \sigma_0^*)(1 - D)^p \tag{6.22}$$

where p is a material parameter. The process of cyclic loading is described by the time variation of stress in the following form

$$\sigma(t) = \frac{1}{2}\sigma_{\mathrm{a}}[1 + \sin(\omega t)], \qquad \omega = \frac{2\pi}{T}, \tag{6.23}$$

where σ_{a} is the stress amplitude. Substitution of σ from Eq. (6.23) into Eq. (6.21) and integration lead to the equation of damage increase in a single cycle that can be expressed as follows

$$\int_0^{\widetilde{D}} (1 - D)^{np} dD = \frac{A\omega\sigma_a}{2(\sigma_{\mathrm{c}}^* - \sigma_0^*)^{n+1}} \int_0^T \left\{\frac{1}{2}\sigma_a[1 + \sin(\omega t)] - \sigma_0^*\right\}^n \cos(\omega t) dt \tag{6.24}$$

Finally, damage evolution law for single cycle takes the form:

$$\widetilde{D} = 1 - \left\{1 - \frac{A\omega\sigma_a}{2(\sigma_{\mathrm{c}}^* - \sigma_0^*)^{n+1}} \left[\left(\frac{1}{2}\sigma_{\mathrm{a}}[1 + \sin(\omega t)] - \sigma_0^*\right)^{n+1} - \left(\frac{1}{2}\sigma_{\mathrm{a}} - \sigma_0^*\right)^{n+1}\right]\right\}^{\frac{1}{pn+1}} \tag{6.25}$$

The free edges of the sample due to surface irregularities act as a kind of stress concentrators. The influence of edge defects on the damage evolution and crack propagation is significant.

In order to account for the edge effect, the stress fluctuation function (see Fig. 6.36) is introduced and the total stress expressed as follows

$$\sigma(x) = \bar{\sigma} + \tilde{\sigma}(x) = \bar{\sigma} + \bar{\sigma} y(x) = \bar{\sigma}\left(1 + \alpha + \beta\left|\frac{x}{a}\right|^m\right) \tag{6.26}$$

where $y(x)$ denotes the fluctuation function, a is the width of the sample, β and m are the material parameters. The integration of stress fluctuation on $[0, a]$ makes possible to establish α parameter

$$\int_0^a \tilde{\sigma}(x)dx = 0 \quad \rightarrow \quad \int_0^a \left(\alpha + \beta \left|\frac{x}{a}\right|^m\right) dx = 0 \quad \rightarrow \quad \alpha = -\frac{\beta}{m+1} \tag{6.27}$$

Boundary condition at the external edge allows to designate β parameter

$$\tilde{\sigma}(x = a) = \sigma^b \quad \rightarrow \quad \beta = \frac{\sigma^b}{\bar{\sigma}} \frac{m+1}{m} \tag{6.28}$$

The value of σ^b is assumed to correspond to measured boundary fluctuation, here $\sigma^b = 1.1\bar{\sigma}$. Finally, the stress distribution in expressed in the following form

$$\sigma(x,t) = \bar{\sigma}\left(1 + \alpha + \beta \left|\frac{x}{a}\right|^m\right)\left[\frac{1}{2} + \frac{1}{2}\sin(\omega t)\right] \tag{6.29}$$

According to the mathematical description, the numerical analysis of damage evolution (6.21) under mechanical loads (6.29) in elastic-plastic solids has been made. The evolution of damage during the increasing number of cycles is shown in Fig. 6.37. The macro-crack initiation occurs at the critical value of damage $D_c = 0.3$.

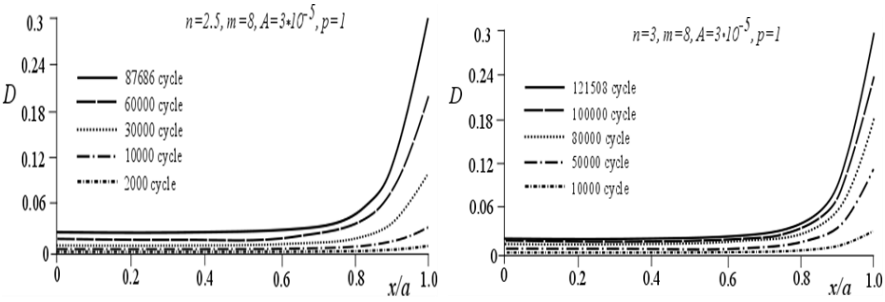

Fig. 6.37 Damage evolution related to the number of cycles for different values of the parameter n

6.4 Alternative Non-destructive Testing Techniques for Damage Identification

6.4.1 Introductory Remarks

In the previous sections the optical nondestructive techniques were presented as the powerful tools for fatigue damage identification. It has to be mentioned however, that there are many other nondestructive testing techniques commonly used for damage assessments (Narayan and Green Jr., 1975; Sablik and Augustyniak, 1999; Marténez-Ona and Pérez, 2000; Ogi et al, 2000; Fel et al, 2001). There are also many destructive methods supporting this issue (Hayhurst, 1972; Trąmpczyński and Kowalewski, 1986; Kowalewski, 2005). Having the parameters of destructive and nondestructive methods for damage development evaluation, it is instructive to analyze their variation in order to find possible correlations. This is because of the fact that typical destructive investigations, like creep, fatigue or standard tensile tests, give the macroscopic parameters characterizing the lifetime, strain rate, yield point, ultimate tensile stress, ductility, etc. without any information concerning microstructural damage development and material microstructure variation. On the other hand, nondestructive methods provide information about damage at a particular time of the entire working period of an element, however, without sufficient information about the microstructure and how it varies with time. Therefore, it seems reasonable to plan future damage development investigations in the form of interdisciplinary tests connecting results achieved using destructive and nondestructive methods with microscopic observations in order to find mutual correlations between their parameters (Dietrich and Kowalewski, 1997; Makowska, 2014).

To assess damage using destructive method, the specimens after different amounts of prestraining are usually stretched up to failure. The selected tensile parameters can be determined afterwards, and their variations can be used for identification of damage development. Ultrasonic and magnetic investigations are often selected as the nondestructive methods for damage development evaluation. In the case of ultrasonic method, the acoustic birefringence coefficient is often used to identify damage development in the steels tested. Two magnetic techniques for the nondestructive testing are especially suitable, i.e., measurement of the Barkhausen effect (HBE) and the magneto-acoustic emission (MAE). Both effects are due to an abrupt movement of the magnetic domain walls depicted from microstructural defects when the specimen is magnetized. The laboratory test specimens are magnetized by a solenoid and the magnetic flux generated in the specimen is closed by a C-core shaped yoke. The magnetizing current (delivered by a current source) has typicaly a triangular waveform and frequency of order 0.1 Hz. Its intensity is proportional to the voltage UG. Two sensors can be used: (a) a pickup coil (PC) and (b) an acoustic emission transducer (AET). A voltage signal induced in the PC is used for the magnetic hysteresis loop $B(H)$ evaluation (low frequency component) as well as for the HBE analysis (high frequency component). The intensity of the HBE is given by the rms (root mean square) voltage U_{b} envelopes. The maximal values (U_{bpp}) of U_{b} for one period of

magnetization can be then compared. An analogous analysis can be performed for the MAE voltage signal from the AET. In this case, the maximal values (U_{app}) of the U_a voltage envelopes are compared. The magnetic coercivity H_c, evaluated from the $B(H)$ hysteresis loop plots, can also be taken into account.

6.4.2 Examples of the Results from Research Programs Executed for Damage Analysis

6.4.2.1 Magnetic Techniques Combined with Destructive Methods

This section describes an application of non-destructive magnetic techniques supporting damage evaluation due to creep or plastic flow on the basis of the selected damage sensitive parameters coming from tensile tests and magnetic investigations carried out on the P91 steel specimens. The low carbon, creep-resistant P91 steel is typically used for tubes, plates and structural components in the power engineering. Two different types of deformation processes were carried out. First, a series of the P91 steel specimens was subjected to creep, and second one to plastic deformation in order to achieve the material with an increasing strain level up to 10%. Subsequently, non-destructive and destructive tensile tests were performed. Magnetic methods based on measurements of magnetoacoustic emission and magnetic hysteresis loop changes were applied. The static tensile tests were carried out in order to evaluate the mechanical parameters variations. It is shown that some relationships between the selected parameters coming from the non-destructive and destructive tests may be formulated.

The magnetoacoustic emission (MAE) technique is based on the analysis of acoustic signals generated in the bulk of the material subjected to alternating magnetic fields (Makowska and Kowalewski, 2015). MAE is generated during the movement of non-180° domain walls (in the case of steels they are 90° domain walls) as a result of local deformations (volume changes) induced by the local change of magnetisation in a material having the non-zero magnetostriction (Buttle et al, 1986). Domain walls are pinned temporarily by microstructural barriers to disable their motion, and then they are released abruptly with an increase of the magnetic field. Grain boundaries, precipitates, dislocation tangles (Jiles, 1998) and voids (Blaow et al, 2007) are microstructural barriers hindering domain walls movement. It was also suggested that irreversible rotation of the domain through angles other than 180° can also contribute to the MAE signal (O'Sullivan et al, 2004). Magnetoacoustic emission accompanies magnetic Barkhausen effect (MBE) that is produced in steels by movement of both 180° and 90° domain walls. Movement of the 180° domain walls (between anti-parallel domains) does not contribute to the generation of elastic waves. Stresses are not generated as the result of 180° domain walls movements or rotations, since the strain along a particular axis is independent on the direction of the magnetic moments if they act along the same axis (Buttle et al, 1986). As a consequence, the movement of 180° domain walls does not affect magnetostrictive

strain (Buttle et al, 1986). An advantage of the MAE method over the MBE method results from the depth of measurements. In the case of MAE it is dependent only on the ability to magnetise the investigated material and easily reaches 10 mm (or even more in special cases) while for MBE it is only 0–1mm due to attenuation of the generated electromagnetic waves (in the kHz range) by eddy currents (Blaow et al, 2007).

Magnetoacoustic emission intensity, coercivity, saturation induction were measured on the plain specimens of the P91 steel (having a cross section 5 mm × 7 mm and gauge length of 40 mm). The specimens were earlier subjected either to creep (T = 773 K, σ = 290 MPa) or plastic deformation (T = 298 K, V = 1mm/min). The loading process of each specimen was carried out to achieve the different strain level. The creep process was interrupted to obtain various deformation levels i.e.: 0.85%, 1.85%, 3.15%, 4.60%, 5.90%, 7.90% and 9.30%, whereas the levels of plastic deformation were as follow: 2.00%, 3.00%, 4.50%, 5.50%, 7.50%, 9.00%, 10.50%.

Envelopes of the magnetoacoustic emission signal were calculated according to the equation:

$$U_{\mathrm{a}}(h) = \sqrt{\frac{\int_0^{\tau} U_{\mathrm{ta1}}^2(t)dt}{\tau}} \tag{6.30}$$

where: $U_{\mathrm{a}}(h)$ is the root mean square voltage from the acoustic wave sensor calculated over an interval τ during which the average magnetic field $U_{\mathrm{ta1}}(t)$ is the output of the sensor. The integral over a half cycle of the magnetic field was calculated as

$$\mathrm{int}(U_{\mathrm{a}}) = \int_{H_{\mathrm{min}}}^{H_{\mathrm{max}}} U_{\mathrm{sa}}(h)dh \tag{6.31}$$

where

$$U_{\mathrm{sa}}(h) = \sqrt{U_{\mathrm{a}}{}^2(h) - U_{\mathrm{ta}}^2} \tag{6.32}$$

and U_{ta} is the root mean square of the background noise voltage. Hysteresis loop changes were characterised by means of coercivity H_C and saturation induction B_S. The magnetic parameters were normalized with respect to their values for the non-deformed specimen ($\mathrm{Int}(U_{\mathrm{a}})_{\mathrm{norm}}, H_{\mathrm{c\,norm}}, B_{\mathrm{s\,norm}}$).

Example envelopes of magnetoacoustic emission are presented in Fig. 6.38. The MAE envelope of the non-deformed specimen reveals a broad maximum with two peaks (Fig. 6.38a). According to Kwan et al (1984) the first peak on the MAE envelope is mainly due to the creation and the second one to the annihilation of magnetic domains with high contribution of displacement of non-180° domain walls. The changes in the height and width of the peaks in Fig 6.38b, c indicate that magnetoacoustic emission is sensitive to material damage and depends on the type of deformation. The two-peak broad maximum observed in the non-deformed specimen transforms to a single maximum for the specimen strained up to 10.5% in the tensile test (Fig. 6.38b) as well as for the specimen strained up to 9.3% in the creep test (Fig. 6.38c). It can be also noted that the single maximum for the specimen after plastic

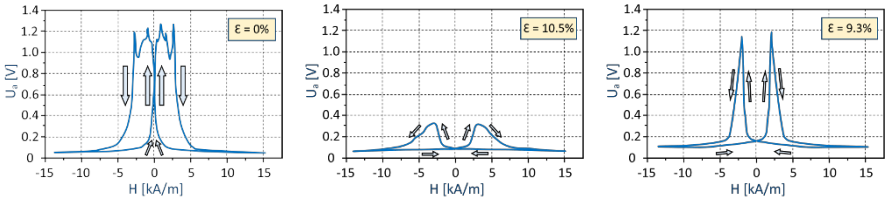

Fig. 6.38 The magnetoacoustic emission rms envelopes for specimens of the P91 steel: a) non-deformed, b) after plastic deformation up to 10.5%, c) after creep up to 9.3% (Makowska et al, 2014)

deformation is broader and lower than for the specimen after creep (Fig. 6.38b, c), which will be discussed later. It can also be seen that the maxima of both envelopes of strained specimens (by creep and plastic deformation) occur at a higher magnetizing field than the maximum of the non-deformed specimen.

Possible explanation is related to the necessity of usage a higher magnetic field to be able to move domain walls in the material with a higher density of dislocations. Transformation of the peak shape for all deformed specimen occurs. The integrals of half-period voltage signals from the magnetoacoustic emission rms envelopes for each specimen were calculated. They are presented in Fig. 6.39.

The integral of the half-period voltage signal of the MAE $\mathrm{Int}(U_\mathrm{a})_\mathrm{norm}$ decreases with the increase of strain level for both plastic and creep deformations, but the dynamics of these processes are different—lower values of this parameter (for deformation values greater than ε = 2%) were obtained for specimens after plastic deformation (Fig. 6.39). The integral of the MAE is almost insensitive to creep in the range of strain between 0.85% and 9.3%. The decrease of both parameters may be explained on the basis of previous knowledge provided by other researchers (Augustyniak, 2003; Augustyniak et al, 2008). The plastic deformation produces defects inside the martensite plates in the form of dislocation tangles that decrease signif-

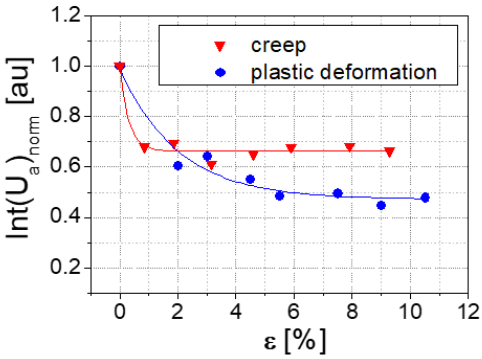

Fig. 6.39 Integral of half-period voltage signal of magnetoacoustic emission versus pre-strain for the P91 steel

icantly the mobility of 'non-180°' domain walls (Augustyniak, 2003). An increase in dislocations density reduces the mean free path of the domain walls displacement and increases their pinning force (Augustyniak et al, 2008). According to the Granato-Lucke theory, it is believed that the ends of the dislocations lines are fastened at points of strong and weak fixation. The points of strong fixation are the nodes of the dislocation network, whereas the points of weak fixation are impurity atoms (Baldev et al, 2001). Under applied stresses the dislocations segments bend between the points of weak fixation. In the case, when the stress exceeds a defined value, the dislocation segment breaks away from the points of weak fixation (Baldev et al, 2001). As a result, due to the dislocation structure modification, movement of the domain walls becomes less effective and the MAE intensity signal and its parameters Int(U_a) decrease monotonically (Blaow et al, 2007).

Usually, in the case of creep of metallic materials, two main processes are dominant: strain hardening and thermal softening (also called as recovery) (Bailey, 1935; Zakharov et al, 2013). The same situation takes place in the P91 steel. The material recovery occurs by dislocation cross slip and dislocation climb. As a result of recovery and relatively high level of acting stress equal to 290 MPa, polygonization of the material occurs thanks to the dislocation climb mechanism. The second important process involved during creep of the P91 steel is the hardening caused by introduction of high density dislocation tangles to the material structure. Therefore, the accelerated creep is a mixed process consisting of creep and plastic components of deformation due to the high level of stress applied. Similarly, for plastic deformation, the movement of the domain walls is impeded due to the significant amount of defects introduced to the material. However, a lesser decrease in the $\mathrm{Int}(U_a)_{\mathrm{norm}}$ values for specimens after accelerated creep than for specimens after tensile tests was observed due the applied temperature (773 K).

The results of mechanical tests conducted on specimens with prior deformation were used to determine the yield point and ultimate tensile stress variations. They demonstrate the softening effect in the P91 steel after creep, whereas after plastic deformation a hardening effect can be observed.

The main aim of the research program was to find relationships between damage sensitive parameters of tensile tests and those determined from magnetic investigations. Representative results are shown in Figs. 6.40 - 6.42. They show the relationships between the ultimate tensile stress and selected magnetic parameters.

Similarly to the results obtained for the yield stress in the case of plastic deformation, the exponential relationships between the ultimate tensile stress and magnetoacoustic emission integral can be observed in the strain levels considered (0–9%) here, Fig. 6.40. It has to be noted however, that for the steel after creep the mutual relationship between these parameters cannot be expressed as a function, since the points representing increasing level of deformation are not located in the orderly manner. The same types of relationships were found between the ultimate tensile stress and coercivity, Fig. 6.41. Contrary to these results, variations of the saturation induction $B_{\mathrm{s\,norm}}$ allow an estimation of the ultimate tensile stress of the P91 steel either after creep (in the whole range) or plastic deformation (range 0 – 9%), Fig.

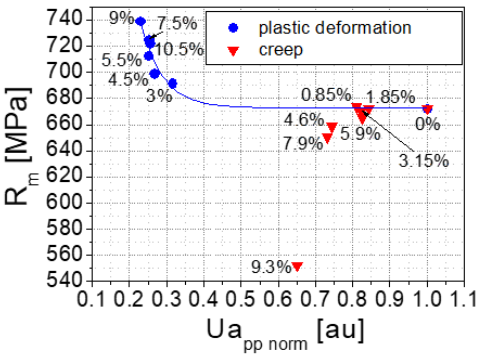

Fig. 6.40 Variation of ultimate tensile stress of the P91 steel versus amplitude of magnetoacoustic emission $U a_{\mathrm{pp\,norm}}$

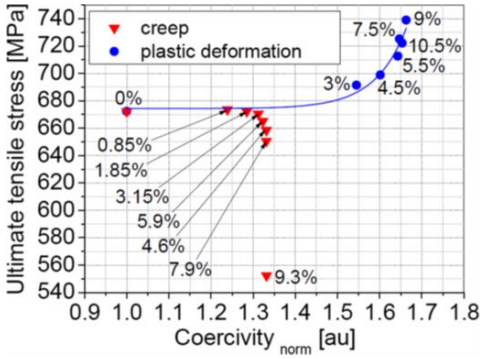

Fig. 6.41 Variation of ultimate tensile stress of the P91 steel versus coercivity $H_{\mathrm{c\,norm}}$

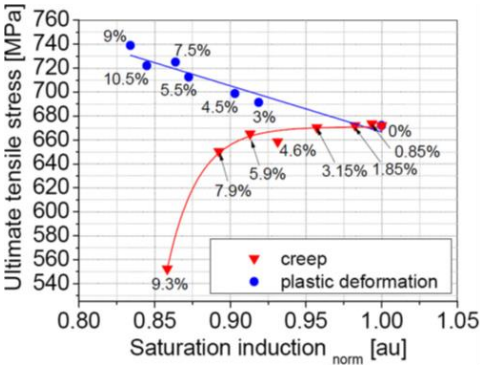

Fig. 6.42 Variation of ultimate tensile stress of the P91 steel versus saturation induction $B_{\mathrm{s\,norm}}$

6.42. The relation $R_{\mathrm{m}} = f(B_{\mathrm{s\,norm}})$ for the material after plastic deformation can be described by the linear function, whereas that after creep, by the exponential one.

6.4.2.2 Ultrasonic Techniques Combined with Destructive Tests

It has been found that various ultrasonic techniques can be applied to evaluate the quality of the material in the as-received state and after deformation history induced by creep, fatigue or plastic flow. Mutual relationships between parameters of ultrasonic waves and those characterising creep were observed in the past (Frost and Ashby, 1982; Brathe, 1978). Variations of nonlinear acoustic parameters were investigated during creep (Ohtani et al, 2006). In late creep stages, when numerous voids were created in the bulk steel specimens, an ultrasonic technique based on acoustic birefringence was used to detect material damage (Kim et al, 2009).

Measurement of acoustic birefringence and evaluation of magnetic parameters seem to be able to provide more comprehensive material degradation data than the replica technique and destructive tests. Acoustic birefringence can be measured using ultrasonic echo technique, for elements accessible from one side only (like pipes for example). Its value is proportional to the difference in the round-trip travel time of ultrasonic pulses polarized in the direction parallel and perpendicular to the loading direction and, at the same time, perpendicular to the loading direction of the specimen. It can be calculated as (Szelązek et al, 2009; Schneider, 1995):

$$B = 2\frac{V_\mathrm{p} - V_\mathrm{l}}{V_\mathrm{l} + V_\mathrm{p}} = 2\frac{t_\mathrm{l} - t_\mathrm{p}}{t_\mathrm{l} + t_\mathrm{p}},$$

where: V_p velocity of shear wave polarized along the loading axis, V_l velocity of shear wave polarized perpendicularly to the loading axis, t_l time of flight of the shear wave polarized along the loading axis, t_p time of flight of the shear wave polarized perpendicularly to the loading axis.

The value of acoustic birefringence depends on various factors influencing the velocity of ultrasonic waves. One can indicate a material texture (preferred grain orientations), concentration and orientation of voids (if any), impurities and dislocation in the bulk of the material, and applied residual stresses in the material.

The advantage of acoustic birefringence measurements is the fact that there is no need to know the exact thickness of the element under test. They do not depend on temperature and they deliver information averaged over the element thickness. Because of these features, this technique has found a wide application in ultrasonic residual stress evaluation in the rims of mono-block railway wheels (Schramm et al, 1996).

Ultrasonic measurements were performed in five spots on each specimen along gauge length. In this way, in specimens exhibiting necking, the maximal value of acoustic birefringence coefficient could be found. Measurements were taken with a 5 MHz shear wave piezoelectric transducer coupled to the specimen surface by means of the viscous epoxy couplant. Spots for measurements performed with ultrasonic techniques on the specimen are presented in Fig. 6.43. The same specimens as those used in magnetic investigations were considered.

It is shown, that also selected ultrasonic damage sensitive parameters can be correlated with the mechanical ones. In our case we have found the acoustic birefringence

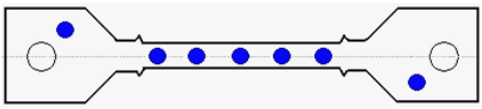

Fig. 6.43 Spots of ultrasonic measurements

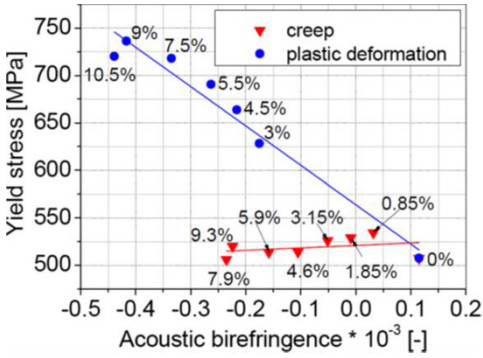

Fig. 6.44 Variation of the yield stress for the P91 steel versus acoustic birefringence

coefficient as that which gives very promising results. Figure 6.44 well summarises some achievements in this area. It illustrates mutual relationship between the acoustic birefringence coefficient and yield stress. The numbers in figure denote the level of prior deformation. The yield stress of the P91 steel after deformation induced by creep almost does not change with the acoustic birefringence coefficient. In the case of prior plastic deformation the yield stress decreases linearly with an increase of the acoustic birefringence coefficient.

6.4.3 Application of Magnetic Techniques in Real Structural Elements for Rapid Inspection

The Barkhausen noise method, based on the measurement of voltage pulses generated by the magnetic domains moving due to the variable magnetic field (Buttle et al, 1986), is regarded as a promising research tool for assessing a degradation of the ferromagnetic materials used particularly in constructions for power engineering. Such a thesis is justified by the numerous papers describing the possibility of determining by this method a degree of material damage in various stages of creep (Palma et al, 2003; Mitra et al, 2007; Mohapatra et al, 2008; Makowska et al, 2014), fatigue (Palma et al, 2003; Sagar et al, 2005) or stress/strain assessment during plastic deformation due to tension (Stupakov et al, 2007; Piotrowski et al, 2009).

The 9Cr-1Mo (0.09% C) steel was tested under creep conditions ($p = 125$ MPa and $T = 600^\circ$ C) (Mitra et al, 2007). The results showed, that the rms of the Barkhausen signal decreased in the primary creep, in the secondary period it dropped reaching the minimum, and then strongly increased. In the tertiary stage, its value increased slightly, taking almost linear relationship with respect to time.

The Barkhausen noise parameter was also determined during fatigue of the SAE8620 steel. It increased with the increasing number of fatigue cycles, and stress amplitude as well. Stupakov et al (2007) investigated the low-carbon steel CSN12013 (C = 0.03%) subjected to plastic deformation up to 23% approximately. It was found that with the increase of plastic deformation (up to 2.5%), the effective voltage of the Barkhausen emission increased, and subsequently decreased. Just mentioned examples of the research programs and their results show that the Barkhausen noise parameters can be successfully used to identify degradation progress of materials in power engineering elements. Applicability of this technique was also confirmed by our investigations in which a degree of degradation of the turbine blade material was tested. A relationship between the time of turbine blade degradation and Barkhausen noise signal was found (Makowska et al, 2017). The tests were carried out for the area of leading edge of the blade and those for the trailing edge part, Fig. 6.45. The representative results were summarized in Figs. 6.46-6.48. They show the results of the Barkhausen noise amplitude for blades after different values of the exploitation time. The values of this parameter indicate that for the blades after longest exploita-

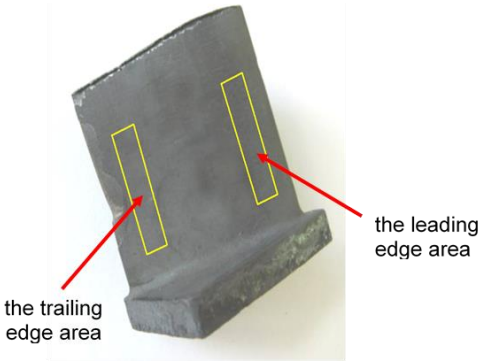

Fig. 6.45 General view of the turbine blade fragment (material: X22CrMoV12-1 (St12T)) showing places of the magnetic investigations

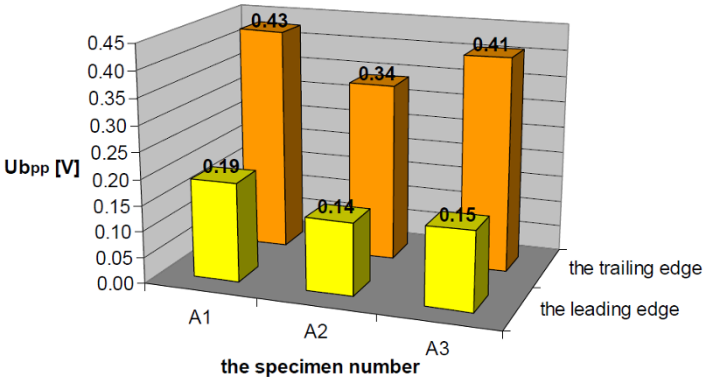

Fig. 6.46 The voltage difference (amplitude Ubpp) between maximum peak value of magnetic Barkhausen emission (Ub) and its background noise (Utb) for blades after 26400 [h] of exploitation

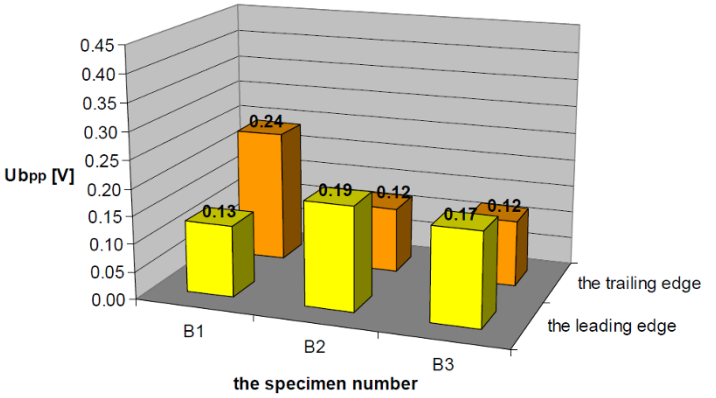

Fig. 6.47 The voltage difference (amplitude Ubpp) between maximum peak value of magnetic Barkhausen emission (Ub) and its background noise (Utb) for blades after 36100 [h] of exploitation

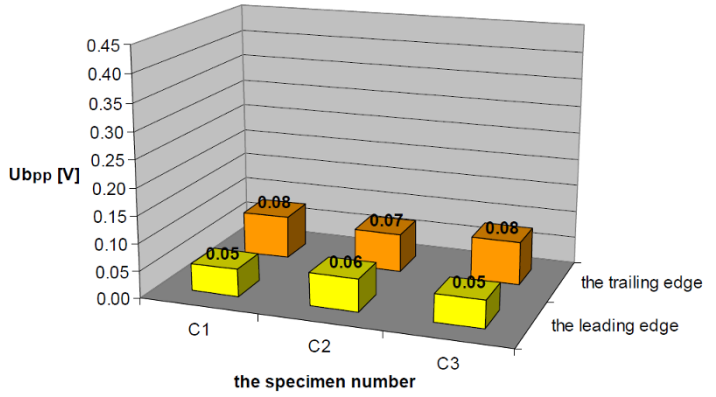

Fig. 6.48 The voltage difference (amplitude Ubpp) between maximum peak value of magnetic Barkhausen emission (Ub) and its background noise (Utb) for blades after 39800 [h] of exploitation

tion period considered here a significant lowering of the Barkhausen signal noise can be obseved in comparison to that obtained for the blades after 26400 hours of exploitation. Examination of blades A1-A3, Fig. 6.46, proves that in the case of blades without visible defects the Barkhausen noise captured on the leading edge was always proportionally lower than that on the trailing edge. This is also confirmed by the results for blades C1 - C3, Fig. 6.48.

In conclusion one can say that the Barkhausen noise method is quite sensitive to the material degradation. The tests enabled to observe the Barkhausen signal level decrease evaluated in the cracks vicinity located on the trailing edge of the blades. The lowest amplitude of the Barkhausen noise was observed for blades that suffered on structural degradation accumulated due to stress state variation around the defects in the form of blade material loss. The results achieved indicate that the Barkhausen

noise method may in the future serve as an alternative technique for damage degree evaluation of selected components working in power engineering. At the current stage of the method development and taking into account a lack of the adequate standards of the presented concept, a further intensive investigations are needed for significantly larger number of cases.

6.5 Closing Remarks and Conclusions

The chapter presents selected results of damage development investigations due to various loading types obtained by means of destructive and nondestructive testing techniques.

The fatigue or creep tests for a range of different materials were interrupted for selected stages in order to assess a damage degree. As destructive methods the standard tensile tests were carried out after prestraining. Subsequently, an evolution of the selected tensile parameters was taken into account for damage identification.

The results of nondestructive tests show that the selected ultrasonic and magnetic parameters can be good indicators of material degradation and can help to locate the regions where material properties are changed due to prestraining.

Taking into account ultrasonic methods, in order to evaluate damage progress in specimens made of the steels, instead of velocity and attenuation measurement, the acoustic birefringence measurements were successfully applied. In the case of magnetic investigations for damage identification the measurements of the Barkhausen effect (HBE) and the magneto-acoustic emission (MAE) were applied. Both effects show that the magnetic properties are highly influenced by prior deformation, and moreover, they are sensitive not only to the magnitude of prior deformation, but also to the way it is introduced.

Among nondestructive methods the relatively novel optical techniques were used for damage initiation and further crack propagation monitoring. The results of damage monitoring during fatigue tests supported by Digital Image Correlation or Electronic Spackle Pattern Interferometry proved their great suitability for effective identification of places of damage initiation.

The results show that ultrasonic and magnetic damage sensitive parameters can be correlated with those coming from destructive tests. It is shown that good correlation of mechanical and selected non-destructive parameters identifying damage can be achieved for the materials in question.

This study suggests that experimental investigations concerning creep and fatigue problems should be based on the interdisciplinary tests, connecting parameters assessed by classical macroscopic destructive investigations, plus microscopic observations with parameters coming from the non-destructive investigations.

The chapter additionally presents simulation of fatigue crack initiation for cyclic loading within the nominal elastic regime. It is assumed that damage growth occurs due to action of mean stress and its fluctuations induced by crystalline grain inho-

mogeneity and free boundary effect. The simulations were supported by the results captured by ESPI system.

References

Andersson M (2013) The influence of notches on fatigue of heat treated sintered steel. In: International Powder Metallurgy Congress and Exhibition, Euro PM 2013 in Gothenburg on September 17, 2013

Augustyniak B (2003) Magnetomechanical effects and their application in nondestructive evaluation of materials (in Polish). Gdansk University of Technology, Gdańsk

Augustyniak B, Chmielewski M, Piotrowski L, Kowalewski Z (2008) Comparison of properties of magnetoacoustic emission and mechanical barkhausen effects for P91 steel after plastic flow and creep. IEEE Transactions on Magnetics 44(11):3273–3276, DOI 10.1109/TMAG.2008.2002525

Bailey RW (1935) The utilization of creep test data in engineering design. Proceedings of the Institution of Mechanical Engineers 131(1):131–349, DOI 10.1243/PIME_PROC_1935_131_012_02

Baldev R, Jayakumar T, Moorthy V, Vaidyanathan S (2001) Characterization of microstructures, deformation and fatigue damage in different steels using magnetic Barkhausen emission technique. Russian Journal of Nondestructive Testing 37(11):789–798, DOI 10.1023/A:1015847303916

Bennett JA, Weinberg JG (1954) Fatigue notch sensitivity of some aluminium alloys. Journal of Research of the National Bureau of Standards 52(5):235–245

Blaow A, Evans JT, Shaw BA (2007) The effect of microstructure and applied stress on magnetic Barkhausen emission in induction hardened steel. Journal of Materials Science 42(12):4364–4371, DOI 10.1007/s10853-006-0631-5

Boronski D (2007) Methods for examination of strain and stress under fatigue of material and structures (in Polish). Report, Institute for Sustainable Technologies - National Research Institute, Bydgoszcz-Radom

Brathe L (1978) Macroscopic measurements of creep damage in metals. Scandinavian Journal of Metallurgy 7(5):199–203

Buttle DJ, Briggs GAD, Jakubovics JP, Little EA, Scruby CB, Busse G, Sayers CM, Green RE, Ash EA, Scruby CB (1986) Magnetoacoustic and Barkhausen emission in ferromagnetic materials. Philosophical Transactions of the Royal Society of London Series A, Mathematical and Physical Sciences 320(1554):363–378, DOI 10.1098/rsta.1986.0124

Chen C (2004) General theory. ME631 15 pages, UAF

Chu TC, Ranson WF, Sutton MA, Peters WH (1985) Application of digital-image-correlation techniques to experimental mechanics. Experimental Mechanics 25(3):232–244, DOI 10.1007/BF02325092

DANTEC (2019) Dynamic info-materials. https://www.dantecdynamics.com/

Dietrich L, Kowalewski ZL (1997) Experimental investigation of an anisotropy in copper subjected to predeformation due to constant and monotonic loadings. International Journal of Plasticity 13(1):87 – 109, DOI 10.1016/S0749-6419(97)00002-8

Dietrich L, Grzywna P, Kukla D (2012) The use of optical methods to locate fatigue damage (in Polish). Przegląd Spawalnictwa 13:15–18

DuQuensay DL, Topper TH, Yu MT (1986) The effect of notch radius on the fatigue notch factor and the propagation of short cracks. In: Miller KJ, de los Rios ER (eds) The behaviour of short fatigue cracks, Mechanical Engineering Publications, London, pp 323–335

Durif E, Réthoré J, Combescure A, Fregonese M, Chaudet P (2012) Controlling stress intensity factors during a fatigue crack propagation using digital image correlation and a load shedding procedure. Experimental Mechanics 52(8):1021–1031, DOI 10.1007/s11340-011-9552-6

Fatemi A, Fang D, Zeng Z (2002) Notched fatigue behaviour under axial and torsion loads: experiment and predictions. In: 8th International Fatigue Congress, Stockholm, vol 3, pp 1905–1914

Fatemi A, Zeng Z, Plaseied A (2004) Fatigue behavior and life predictions of notched specimens made of qt and forged microalloyed steels. International Journal of Fatigue 26(6):663 – 672, DOI 10.1016/j.ijfatigue.2003.10.005

Fel D, Hsu DK, Warchol M (2001) Simultaneous velocity, thickness and profile imaging by ultrasonic scan. Journal of Nondestructive Evaluation 8(3):95–112, DOI 10.1023/A:1013550921673

Filippini M (2000) Stress gradient calculations at notches. International Journal of Fatigue 22(5):397 – 409, DOI 10.1016/S0142-1123(00)00010-4

Forster J, Theobald A, Engel S, Pasmann R (2012) Using optical measuring system for identification of material parameters for finite element analysis. In: 11. LS-DYNA, DYNAmore GmbH, Ulm, pp 1–9

Frost HJ, Ashby M (1982) Deformation-mechanism Maps. The Plasticity and Creep of Metals and Ceramics. Pergamon Press, Oxford, New York, Sydney

GOM (2007) ARAMIS user manual software

Gower MR, Shaw RM (2010) Towards a planar cruciform specimen for biaxial characterisation of polymer matrix composites. In: Advances in Experimental Mechanics VII, Trans Tech Publications Ltd, Applied Mechanics and Materials, vol 24, pp 115–120, DOI 10.4028/www.scientific.net/AMM.24-25.115

Gungor S (2009) Moire interferometry. In: Eaton-Evans J, Dulie-Barton JM, Burguete RL (eds) Modern Stress and Strain Analysis. A State of the Art Guide to Measurement Techniques, British Society for Strain Measurement, pp 8–9

Hayhurst D (1972) Creep rupture under multi-axial states of stress. Journal of the Mechanics and Physics of Solids 20(6):381 – 382, DOI 10.1016/0022-5096(72)90015-4

Jiles D (1998) Introduction to Magnetism and Magnetic Materials, 2nd edn. Taylor and Francis Group, New York

Kamaya M, Kawakubo M (2011) A procedure for determining the true stress–strain curve over a large range of strains using digital image correlation and finite element

analysis. Mechanics of Materials 43(5):243 – 253, DOI 10.1016/j.mechmat.2011.02.007

Kim CS, Park IK, Jhang KY (2009) Nonlinear ultrasonic characterization of thermal degradation in ferritic 2.25Cr–1Mo steel. NDT & E International 42(3):204 – 209, DOI 10.1016/j.ndteint.2008.09.002, 2nd International Conference on Advanced Nondestructive Evaluation

Kopeć M, Grzywna P, Kukla D, Kowalewski Z (2012) Evaluation of the fatigue damage development using ESPI method. Inzynieria Materiałowa 4(212):1–4

Kowalewski ZL (2005) Creep of Metals – Experiment and Modeling (in Polish). IPPT PAN, Warsaw

Kwan MM, Ono K, Shibata M (1984) Magnetomechanical acoustic emission of ferromagnetic materials at low magnetization levels (type I behaviour). Journal of Acoustic Emisssion 3:144–156

Lanning DB, Haritos GK, Nicholas T (1999) Influence of stress state on high cycle fatigue of notched Ti-6Al-4V specimens. International Journal of Fatigue 21:S87 – S95, DOI 10.1016/S0142-1123(99)00059-6

Lord JD (2009) Digital image correlation (dic). In: Eaton-Evans J, Dulie-Barton JM, Burguete RL (eds) Modern Stress and Strain Analysis. A State of the Art Guide to Measurement Techniques, British Society for Strain Measurement, pp 14–15

Makowska K (2014) Methodology for assessing the state of damage to materials subjected to laboratory simulated operational loads (in Polish). PhD Thesis, Instytut Podstawowych Problemów Techniki PAN, Warsaw

Makowska K, Kowalewski ZL (2015) Possibilities of using Barkhausen noise to assess microstructure and mechanical properties of materials (in Polish). Energetyka - Problemy energetyki i gospodarki paliwowo-energetycznej 736(10):664–667

Makowska K, Kowalewski ZL, Augustyniak B, Piotrowski L (2014) Determination of mechanical properties of P91 steel by means of magnetic Barkhausen emission. Journal of Theoretical and Applied Mechanics 52(1):181–188

Makowska K, Kowalewski ZL, Ziółkowski P, Badur J (2017) Assessment of damage level of turbine blades using the Barkhausen noise signal (in Polish). Energetyka-Problemy energetyki i gospodarki paliwowo-energetycznej 760(10):638–641

Marténez-Ona R, Pérez MC (2000) Research on creep damage detection in reformer tubes by ultrasonic testing. In: Proc. 15 WCNDT Roma 2000

Maruno Y, Miyahara H, Noguchi H, Ogi K (2003) Notch size effects in the fatigue characteristics of Al-Si-Cu-Mg cast alloy. Journal of the Japan Institute of Metals 67(7):331–335, DOI 10.2320/jinstmet1952.67.7_331

Mazdumar PK, Lawrence Jr FV (1981) An analytical study of the fatigue notch size effect. A report of the fracture control program, College of Engineering, University of Illinois, Urbana, Illinois

Milke JG, Beuth JL, Biry NE (2000) Notch strengthening in titanium alumini dies under monotonic loading. Experimental Mechanics 40(4):415–424, DOI 10.1007/BF02326488

Mitra A, Mohapatra JN, Swaminathan J, Ghosh M, Panda AK, Ghosh RN (2007) Magnetic evaluation of creep in modified 9Cr–1Mo steel. Scripta Materialia 57(9):813 – 816, DOI 10.1016/j.scriptamat.2007.07.004

Mohapatra J, Ray A, Swaminathan J, Mitra A (2008) Creep behaviour study of virgin and service exposed 5Cr–0.5Mo steel using magnetic Barkhausen emissions technique. Journal of Magnetism and Magnetic Materials 320(18):2284 – 2290, DOI 10.1016/j.jmmm.2008.04.152

Mróz Z, Seweryn A, Tomczyk A (2005) Fatigue crack growth prediction accounting for the damage zone. Fatigue & Fracture of Engineering Materials & Structures 28(1-2):61–71, DOI 10.1111/j.1460-2695.2004.00829.x

Narayan R, Green Jr RE (1975) Ultrasonic attenuation monitoring of fatique damage in nuclear pressure vessel steel at high temperature. In: Materials Evaluation, 25-26 February 1975

Neuber H (1961) Theory of Notch Stresses. Office of Technical Services, U.S. Department of Commerce, Washington, D.C.

Neuber H (2001) Kerbspannungslehre, 4th edn. Klassiker der Technik, Springer, Berlin, Heidelberg

Ogi H, Minami Y, Aoki S, Hirao M (2000) Contactless monitoring of surface-wave attenuation and nonlinearity for evaluating remaining life of fatigued steel. In: Proc. 15 WCNDT Roma 2000

Ohtani T, Ogi H, Hirao M (2006) Evolution of microstructure and acoustic damping during creep of a Cr–Mo–V ferritic steel. Acta Materialia 54(10):2705 – 2713, DOI 10.1016/j.actamat.2006.02.010

Olszak W (1965) Theory of Plasticity (in Polish). PWN, Warsaw

O'Sullivan D, Cotterell M, Cassidy S, Tanner DA, Mészáros I (2004) Magneto-acoustic emission for the characterisation of ferritic stainless steel microstructural state. Journal of Magnetism and Magnetic Materials 271(2):381 – 389, DOI 10.1016/j.jmmm.2003.10.004

Palma ES, Júnior AA, Mansur TR, Pinto JMA (2003) Fatigue damage in AISI/SAE 8620 steel. In: Proceedings of COBEM 2003, 17th International Congress of Mechanical Engineering, 10-14 November, São Paulo, Brazil

Patorski K (2005) Laser Interferometry (in Polish), Oficyna Wydawnicza Politechniki Warszawskiej, Warsaw, pp 214–261

Peterson RE (1959) Analytical approach to stress concentration effect in fatigue of aircraft materials. In: Proceedings on Fatigue of Aircraft Structure, no. 59-507 in WADC Technical Report, pp 273–299

Pierron S (2009) Digital speckle pattern interferometry. In: Eaton-Evans J, Dulie-Barton JM, Burguete RL (eds) Modern Stress and Strain Analysis. A State of the Art Guide to Measurement Techniques, British Society for Strain Measurement, pp 14–15

Pilkey WD (1997) Peterson's Stress Concentration Factors. Wiley, New York

Piotrowski L, Augustyniak B, Chmielewski M, Tomáš I (2009) The influence of plastic deformation on the magnetoelastic properties of the CSN12021 grade steel. Journal of Magnetism and Magnetic Materials 321(15):2331 – 2335, DOI 10.1016/j.jmmm.2009.02.028

Pluvingae G (2001) Notch effects in fatigue and fracture. In: Pluvingae G, Gjonaj M (eds) Notch Effects in Fatigue and Fracture, Springer Science + Business

Media, Dordrecht, NATO Science Series (Series II: Mathematics, Physics and Chemistry), vol 11, pp 1–22

Qian G, Hong Y, Zhou C (2010) Investigation of high cycle and very-high-cycle fatigue behaviors for a structural steel with smooth and notched specimens. Engineering Failure Analysis 17(7):1517 – 1525, DOI 10.1016/j.engfailanal.2010.06.002

Sablik MJ, Augustyniak B (1999) Magnetic methods of nondestructive evaluation. In: Wiley Encyclopedia of Electrical and Electronics Engineering, Wiley, DOI 10.1002/047134608X.W4552

Sagar SP, Parida N, Das S, Dobmann G, Bhattacharya DK (2005) Magnetic Barkhausen emission to evaluate fatigue damage in a low carbon structural steel. International Journal of Fatigue 27(3):317 – 322, DOI 10.1016/j.ijfatigue.2004.06.015

Schneider E (1995) Ultrasonic birefringence effect — Its application for materials characterisations. Optics and Lasers in Engineering 22(4):305 – 323, DOI 10.1016/0143-8166(94)00032-6

Schramm RE, Szelązek J, Clark Jr AV (1996) Ultrasonic measurement of residual stress in the rims of inductively heated railroad wheels. Material Evaluation 54:929–934

Siebel E, Stieler M (1955) Ungleichformige Spannungsverteilung bei schwingender Beanspruchung. VDI Zeitschrift 97(5):121–126

da Silva BL, Ferreira JLA, Araújo JA (2012) Influence of notch geometry on the estimation of the stress intensity factor threshold by considering the Theory of Critical Distances. International Journal of Fatigue 42:258 – 270, DOI 10.1016/j.ijfatigue.2011.11.020, fatigue Damage of Structural Materials VIII

Stupakov O, Pal'a J, Tomáš I, Bydžovský J, Novák V (2007) Investigation of magnetic response to plastic deformation of low-carbon steel. Materials Science and Engineering: A 462(1):351 – 354, DOI 10.1016/j.msea.2006.02.475, international Symposium on Physics of Materials, 2005

Szelązek J, Mackiewicz S, Kowalewski ZL (2009) New samples with artificial voids for ultrasonic investigation of material damage due to creep. NDT & E International 42(2):150 – 156, DOI 10.1016/j.ndteint.2008.11.004

Szymczak T (2018) Investigations of material behaviour under monotonic tension using a digital image correlation system. Journal of Theoretical and Applied Mechanics 56(3):857–871, DOI 10.15632/jtam-pl.56.3.857

Szymczak T, Grzywna P, Kowalewski ZL (2013) Modern methods for determining the strength properties of construction materials (in Polish). Transport Samochodowy 1:79–104

Topper T, M Wetzel R, Dean Morrow J (1967) Neuber's rule applied to fatigue of notched specimens. Report NAEC-ASL-1114, Aeronautical Structures Laboratory

Toussaint F, Tabourot L, Vacher P (2008) Experimental study with a digital image correlation (DIC) method and numerical simulation of an anisotropic elastic-plastic commercially pure titanium. Archives of Civil and Mechanical Engineering 8(3):131 – 143, DOI 10.1016/S1644-9665(12)60168-X

Trąmpczyński W, Kowalewski ZL (1986) A tension-torsion testing technique. In: Science EA (ed) Proc. Symp. "Techniques for multiaxial creep testing", London and New York, pp 79–92

Ustrzycka A, Mróz Z, Kowalewski ZL (2017) Experimental analysis and modelling of fatigue crack initiation mechanisms. Journal of Theoretical and Applied Mechanics 55(4), DOI 10.15632/jtam-pl.55.4.1443

Vial-Edwards C, Lira I, Martinez A, Monzenmayer M (2001) Electronic speckle pattern interferometry analysis of tensile tests of semihard copper sheets. Experimental Mechanics 41(1):58–61, DOI 10.1007/BF02323105

Wahl AM, Beuwkes Jr R (1930) Stress concentration produced by holes and notches. Trans ASME APM-56-11:617–623

Westergaard HM (2014) Theory of Elasticity and Plasticity, Harvard Monographs in Applied Science, vol 3. Harvard University Press, Cambridge, MA

Whaley RE (1964) Fatigue and static strength of notched and un-notched aluminium alloy and steel specimens. Experimental Mechanics 2(11):329–334, DOI 10.1007/BF02326137

Zakharov VA, Ul'yanov AI, Gorkunov ES, Velichko VV (2013) Coercive-force hysteresis of carbon steels during elastic cyclic tensile deformation. Russian Journal of Nondestructive Testing 49(5):260–269, DOI 10.1134/S1061830913050070

MARKED PROOF

Please correct and return this set

Please use the proof correction marks shown below for all alterations and corrections. If you wish to return your proof by fax you should ensure that all amendments are written clearly in dark ink and are made well within the page margins.

Instruction to printer	*Textual mark*	*Marginal mark*
Leave unchanged	··· under matter to remain	New matter followed by
Insert in text the matter indicated in the margin		or
Delete	through single character, rule or underline or through all characters to be deleted	or
Substitute character or substitute part of one or more word(s)	through letter or through characters	new character or new characters
Change to italics	under matter to be changed	
Change to capitals	under matter to be changed	
Change to small capitals	under matter to be changed	
Change to bold type	under matter to be changed	
Change to bold italic	under matter to be changed	
Change to lower case	Encircle matter to be changed	
Change italic to upright type	(As above)	
Change bold to non-bold type	(As above)	
Insert 'superior' character	through character or where required	or under character e.g. or
Insert 'inferior' character	(As above)	over character e.g.
Insert full stop	(As above)	
Insert comma	(As above)	
Insert single quotation marks	(As above)	or and/or or
Insert double quotation marks	(As above)	or and/or or
Insert hyphen	(As above)	
Start new paragraph		
No new paragraph		
Transpose		
Close up	linking characters	
Insert or substitute space between characters or words	through character or where required	
Reduce space between characters or words	between characters or words affected	